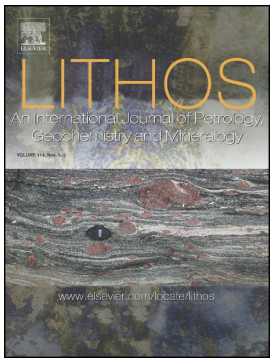


# Crystallochemical indexes and geothermobarometriccalculations as a multiproxy approach to P-Tcondition of the low-grade metamorphism: Thecase of the San Luis Formation, Eastern Sierras Pampeanas of Argentina.

Sebastián O. Verdecchia, Gilda Collo, Priscila S. Zandomeni, Cecilia Wunderlin, Mariano Fehrmann

PII: S0024-4937(18)30442-0
DOI: https://doi.org/10.1016/j.lithos.2018.11.021
Reference: LITHOS 4875

To appear in: *LITHOS*

Received date: 22 May 2018
Accepted date: 17 November 2018

Please cite this article as: Sebastián O. Verdecchia, Gilda Collo, Priscila S. Zandomeni, Cecilia Wunderlin, Mariano Fehrmann , Crystallochemical indexes and geothermobarometriccalculations as a multiproxy approach to P-Tcondition of the low-grade metamorphism: Thecase of the San Luis Formation, Eastern Sierras Pampeanas of Argentina.. Lithos (2018), https://doi.org/10.1016/j.lithos.2018.11.021

# Crystallochemical indexes and geothermobarometric calculations as a multiproxy approach to *P-T* condition of the low-grade metamorphism: the case of the San Luis Formation, Eastern Sierras Pampeanas of Argentina.

Sebastián O. Verdecchia[a,b,*] sverdecchia@unc.edu.ar, Gilda Collo[a,b], Priscila S. Zandomeni[a,b], Cecilia Wunderlin[a,b], and Mariano Fehrmann[c]

[a]Universidad Nacional de Córdoba. Facultad de Ciencias Exactas, Físicas y Naturales. Av. Vélez Sarsfield 1611, X5016CGA. Córdoba, Argentina

[b]Consejo Nacional de Investigaciones Científicas y Tecnológicas (CONICET), Centro de investigaciones en Ciencias de la Tierra (CICTERRA). Av. Vélez Sarsfield 1611, X5016CGA. Córdoba, Argentina

[c]Gobernador Gómez 1383, 9410, Ushuaia, Argentina

[*]Corresponding author at: Centro de investigaciones en Ciencias de la Tierra (CICTERRA). Facultad de Ciencias Exactas, Físicas y Naturales Universidad Nacional de Córdoba, Av. Vélez Sarsfield 1611, X5016CGA. Córdoba, Argentina.

**Abstract**.

In this work, crystallochemical indexes and geothermobarometric calculations are used together to estimate the *P-T* condition in low-grade metamorphic units of the San Luis Formation from Sierra de San Luis (Eastern Sierras Pampeanas of Argentina). Phyllites and slates from this formation record at least two episodes of white mica (Wm) and chlorite (Chl) growth associated with main $D_1$-$S_1$ ($Wm_2$-$Chl_1$) and local $D_2$-$S_2$ ($Wm_3$-$Chl_2$) stages. Mean $KI_{CIS}$ values of 0.30 (Western Belt) and 0.23 Δ°2θ (Eastern Belt) were determined for the <2 μm fraction. Moreover, since the average grain size of the $Wm_2$ exceeds 10 μm, $KI_{CIS}$ values were also measured for the 10-20 μm fraction ranging between 0.22 and 0.24 Δ°2θ for both belts. For those fractions, the $KI_{CIS}$ values indicate epizone conditions, associated with temperatures higher than 300º C. These values are comparable to temperatures obtained from chlorite thermometers, 316º-416º C in Western Belt and 261º-403º C in the Eastern Belt. Pressure values for $D_1$ stage constrained from chlorite – white mica – quartz – $H_2O$ equilibrium are 2.5-5.1 kbar in the Western Belt, and at 3.3-4.7 kbar in Eastern Belt. The pressures are consistent with white mica *b* parameter values measured in samples from Western Belt (9.006 to 9.025 Å) and Eastern Belt (9.003 to 9.020 Å), linked to intermediate thermal gradients (25-35ºC/km).

The identification of increasing *P-T* condition paths in low-grade metasedimentary successions is not easy in the absence of higher grade rocks; in these situations, a systematic sampling and analysis of dozens of samples must be carried out. The very good correlation between crystallochemical index values (Kübler index and white mica *b* parameter) and thermobarometric calculations (empirical and semi-empirical chlorite thermometers and thermobarometry for chlorite – white mica – quartz – $H_2O$ equilibrium) presented in this work argues in favor of the development of a multiproxy study strategy in this type of low-grade metasedimentary successions that involve: (1) a systematic sampling of metapelite

levels for X-ray diffraction study (mineralogical and crystallochemical indexes with a rapid implementation allowing a dense systematic samplig); (2) the recognition of variations in the *P-T* conditions from KI and *b* parameter values and the consequent selection of metapelitic samples for analyzing mineral chemistry and thermobarometric calculations. In order to facilitate these calculations, a user-friendly spreadsheet for crystallochemical indexes and chlorite thermometry calculations is also provided.

**Keywords**: Kübler Index; white mica *b* parameter; chlorite thermometry; multi-equilibrium thermobarometry; Central-Western Argentina.

## 1. Introduction

The thermobarometric determination in quartz-phyllosilicate metapelites or phyllites from low-temperature metamorphism is a great challenge. In this sense, a multiproxy approach, with X-ray diffraction (XRD) measurements and thermobarometric calculations (cf. Warr and Ferreiro Mählmann, 2015; Vidal et al., 2016), could be very helpful. The XRD methods include the measuring of cristallochemical indexes, such as the white mica *b* parameter (Sassi and Scolari, 1974; Guidotti and Sassi, 1986; Guidotti et al., 1989), the Kübler index in white micas (Kübler, 1964; Warr and Rice, 1994; Warr and Ferreiro Mählmann, 2015) or the Árkai index in chlorites (Árkai, 1991). These methods are strongly dependent on the size of the studied fractions, textural features (e.g., small scale bedding composed by quartz plagioclase- and phyllosilicates-rich layers), small scale compositional variations (e.g., Lanari et al. 2012; Cantarero et al. 2014; Scheffer et al. 2016; Airaghi et al. 2017) and experimental parameters, such as shape and material of the sample holder, age of the X-ray tube, geometry of the diffractometer, among others (Kübler and Jaboyedoff, 2000; Abad, 2007). On the other hand, the thermobarometric calculations included empirical and semi-empirical approaches (see summary in Yavuz et al., 2015; Vidal et al., 2016). Chlorite empirical thermometers are commonly based on Al content, tschermak substitution, and octahedral vacancies, showing a systematic behaviour with variation of temperature (e.g., Cathelineau and Nieva, 1985; Jowett, 1991, Hillier and Velde; 1991), even though these thermometers are constrained to low-pressure series (<6 kbar; e.g., Vidal et al., 2001). The semi-empirical calculations incorporate thermodynamic and theoretical approaches, which can be applied in “inverse” and “forward” methods (e.g., Powell and Holland, 2008). In low-grade, the inverse methods allow constraining the formation conditions from the chlorite and/or white mica equilibria in quartz-bearing rocks (see Vidal et al., 2001, 2005, 2006; Inoue et al., 2009, 2018; Dubacq et al., 2010; Bourdelle et al., 2013; Lanari et al., 2014);

however, most of them require knowing the $X\mathrm{Fe}^{+3}$ ratio in the phyllosilicate composition (e.g., Vidal et al., 2016). On the other hand, the phase equilibria modelling should be the best way to determine the *P-T* conditions; however, it requires adequate solution models for phyllosilicate (chlorite and white mica) for low temperature (e.g., Parra et al., 2002; Dubacq et al., 2010; Lanari et al., 2014), which should also include the $\mathrm{Fe}^{+3}$ content (e.g., Vidal et al., 2016; Trincal and Lanari, 2016). Furthermore, if the equilibrium phase diagram construction is applied, it is required to determine a reliable effective (or reactive) bulk composition, discarding detrital phases and the effect of polymorphism and fractionation of the bulk composition (zoned minerals, minerals that do not participate in the reactions; e.g., Stüwe, 1997; Lanari and Engi, 2017).

In this work, XRD methods and geothermobarometric calculations are applied and evaluated through the detailed study of metapelites from two low-grade metasedimentary belts of San Luis Formation (Prozzi, 1990) from Sierra de San Luis (Eastern Sierras Pampeanas of Argentina). This unit was selected due to its structural features, which are relatively simple, with two superposed foliations: the main penetrative $S_1$, parallel to compositional primary bedding ($S_0$), and another $S_2$ locally developed as a crenulation cleavage (see von Gosen, 1998; Gonzalez et al., 2004). In addition, we include a spreadsheet (see Supplementary Table 1) that allows calculating all the used thermometers in a simple way, from semi-empirical and empirical chlorite thermometers compiled from literature, to white mica crystallochemical indexes (Kübler Index and *b* parameter).

## 2. Geology of the San Luis Formation

The metamorphic basement of the Sierra de San Luis (Fig. 1) is commonly divided into three metamorphic complexes, from east to west: Conlara (mid- to high-grade), Pringles (low- to high-grade) and Nogolí (mid- to high-grade) (e.g., Hauzenberger et al., 2001). These

complexes would represent part of the Early Paleozoic evolution of the paleo-margin of southwestern Gondwana (e.g., Steenken et al., 2006; Siegesmund et al., 2010). The San Luis Formation was described alternatively as an independent unit (e.g., von Gosen and Prozzi, 1998; Ortiz Suárez and Casquet; 2005; Morosini et al., 2017) or as part of the Pringles Metamorphic Complex (e.g., Steenken et al., 2006, 2008; Delpino et al., 2015). The San Luis Formation is a low-grade metasedimentary succession exposed in two NNE-SSW belts, here denominated as Eastern and Western belts (Fig. 1), well represented in the south-western region of the Sierra de San Luis. This unit is mainly composed by an alternation of metapelites (slates and phyllites), metapsammites, metaquartzites and scarce metaconglomerates (see von Gosen, 1998; Perón Orrillo and Rivarola, 2014 and references therein), whose protoliths were interpreted as part of a clastic turbiditic sequence (Prozzi, 1990). Detrital zircon U-Pb ages suggest a Mid Cambrian maximum depositional age for protholits (Drobe et al., 2009). On the other hand, the schist succession, in transitional contact with the low-grade rocks in the Western Belt (Fig. 2a), is intruded by the Ordovician Escalerilla granitic pluton (Morosini et al., 2017), thus a minimal Ordovician depositional age is established.

Structurally, the compositional bedding in the San Luis Formation defines the primary $S_0$ plane with NNE trend and WNW-ESE deep dip, which is overprinted by a penetrative $S_1$ metamorphic foliation (Fig. 3; von Gosen, 1998; Gonzalez et al., 2004; Delpino et al., 2015). The $S_1$ plane was widely recognized in west and east low-grade belts, with NNE structural trend and high WNW-ESE deep in relation to axial plane of open to tight folds (von Gosen, 1998; Gonzalez et al., 2004). Locally, a N-NE trend and high NW deep $S_2$ foliation was identified near and sub-parallel to narrow shear zones, mostly located in the E-W limits of the low-grade belts (von Gosen, 1998; von Gosen and Prozzi, 1998; Gonzalez et al., 2004; Morosini and Ortiz Suárez, 2011; Fig. 2). The thermal conditions for the minerals associated

with $D_1$ stage (white mica-chlorite-quartz-plagioclase) were linked to low green schist facies (Gonzalez et al., 2004; Wemmer et al., 2011; Delpino et al., 2015).

## 3. Methods: sampling and analytical procedures

### 3.1. Sampling

The sampling was carried out along two W-E profiles from the Eastern and the Western belts of the San Luis Formation (Fig. 2). In the Western Belt, the profile followed the Nº 9 provincial road near La Carolina town (Fig. 2a); in the Eastern Belt, the profile followed the road that links the Paso del Rey and Santo Domingo localities (Fig. 2b). A total of 22 samples of fine-grained metapelites (slates and phyllites; listed in Table 1) were selected in order to analyse textural and mineralogical relationships, through petrographic descriptions and, in selected samples for electron microprobe (see below), backscattered electron image analysis.

### 3.2. Clay minerals X-ray diffraction (XRD) analyses

The <2 μm fraction was separated for 22 samples of metapelites following the recommendations of Moore and Reynolds (1997). Clay-mineral composition was established by the comparison of orientated aggregates: air-dried (AD), ethylene-glycol solvated (EG), and heated at 500 ºC (HO). X-ray analyses were performed with a Philips PW1800 (Laboratory of Electron Microscopy and X-ray Analysis-LAMARX, Facultad de Matemática, Física y Astronomía, Universidad Nacional de Córdoba-UNC, Argentina) and a X-Pert Pro (Departamento de Físico Química, UNC) diffractometers employing Cu radiation, from 4 to 35° 2θ, with a step size of 0.02° 2θ, a count time of 2 s per step and 40 kV, 40 mA. Clay-mineral phases were semi-quantified using Mineral Intensity Factors (MIF) following the recommendations of Moore and Reynolds (1997). The weight percentages of each clay

mineral present were estimated using the HighScore software and the MIF factors. Those that do not appear between the lists of Moore and Reynolds (1997) were calculated with the NEWMOD© software (Reynolds, 1985) on the base of the intensity relationships of clay minerals referenced to the (003) illite reflection (Moore and Reynolds, 1997). White mica (Wm) was identified by the presence of reflections at ~10 (001), 5 (002) and 3.38 Å (003) in the AD oriented sample diagrams, which do not show modifications in the diagrams of samples treated with Ethylene Glycol nor in the heated ones. The kaolinite was identified by the presence of the reflections at ~7 (001) and 3.58 Å (002), both in the AD and EG diagrams, which disappear in the HO diagrams, after heating the samples to 500 °C for 4 hours. The chlorite was identified by its reflections at ~14 (001), 7 (002), 4.76 (003) and 3.53 Å (004) in the AD diagrams, which are not modified in the EG diagrams, while in the HO diagrams they become less intense. The presence of illite-smectite (I/S) mixed-layers was determined by the reflection near ~11 to 17 º2θ in the EG diagrams and the percentage of white mica in I/S and ordering types (R0, R1 and R3) were determined by the position of the I/S (001-002) and (002-003) reflections in the EG preparations following the recommendations of Moore and Reynolds (1997). The goethite was identified by its more intense reflection at ~4.18 Å; while the reflections located at ~4.26 and 3.34 Å were assigned to quartz. The Kübler Index (KI) was measured in the <2 µm fraction, and in both AD and EG orientated aggregates between 7.5 and 10 º2θ, with a divergent slit of 1º, and 0.5º/min. $KI_{CIS}$ values (Crystallinity Index Standard, Warr and Rice, 1994; Warr and Ferreiro Mählmann, 2015) were established from the regression equation for the X'PertPro diffractometer: $y = 0.812x + 0.0819$ ($R^2 = 0.9833$). $KI_{CIS}$ values were also measured in 2-10 and 10-20 µm fractions from 8 samples that were also analysed by electron microprobe (see below), with the aim of comparing the presence of more than one white mica generation episodes. The white mica *b* parameter (Guidotti and Sassi, 1986) was measured in 20 samples, between 59.25 and 62° 2θ, with a step size of and

0.005° 2θ and a count time of 1 second per step, in rock slices orientated perpendicular to the main foliation. The quartz (211) reflection, positioned at 1.541Å, was used as internal standard. Mineral abbreviations are from Whitney and Evans (2010).

3.3. Mineral chemistry

Chemical analyses of chlorites (n=121) and white mica (n=235) were made in eight metapelitic samples, which were selected because of they present the best foliation development ($S_1$ or $S_1$+$S_2$; see Table 1). These analysis were performed with an electron microprobe (EPMA) JEOL JXA 8230 at the LAMARX, operating in WDS mode, under 15 kV accelerating potential, 10 nA beam current in phyllosilicates, on carbon-coated polished mounts. The beam diameter was between 2 to 10 µm based on the size of the mineral of interest, with counting time of 10 seconds on the peak, and 5 seconds at each background position. In order to decrease the diffusion effect, $Na_2O$ and $K_2O$ were first analysed during 5 seconds on the peak and 2.5 seconds on the background. Mineral compounds were used as standards: Si (forsterite, wollastonite), Al (anorthite, anorthoclase), Fe (fayalite), Mg (forsterite, diopside), Na (anorthoclase), Mn (rodonite), Ti (ilmenite), Ca (wollastonite), F (topaz) and Cl (sodalite).

Structural formulas were calculated for chlorite and white mica on the base of 14 and 11 anhydrous oxygen, respectively. In these minerals, total Fe is expressed as FeO for chemical descriptions, but an initial $XFe^{3+}=Fe^{3+}/(Fe^{3+}+Fe^{2+})$ was assumed for chlorite and white mica in thermobarometric calculations. In chlorite, the $XFe^{3+}$ value was adjusted in a similar way to the approach of Inoue et al. (2018). In this methodological approach, temperatures from thermometers with Fe total as $Fe^{2+}$ + $Fe^{3+}$ (Inoue et al., 2009) and with Fe total as $Fe^{2+}$ (Inoue et al., 2018) should be identical or similar for a set of $XFe^{3+}$. Obtained values between 0.1 and 0.3, with a value of 0.2 in most of chlorite analyses (see

Supplementary Table 2) were used. Similar results were obtained comparing the thermometer of Inoue et al. (2009) and Bourdelle et al. (2013) for analyses that have amounts of vacancies of ($Al^{VI}$-$Al^{IV}$-Na-K)/2 >0.05 apfu (Fe total as FeO). In the white mica, the $XFe^{3+}$ was adjusted from oxide mineral association, following the recommendations of Guidotti et al. (1994). The presence of rutile and ilmenite, and locally of pyrite and graphite, as main accessory associations in most samples, suggests a low-$fO_2$, which is consistent with $XFe^{3+}$ value in white mica of around 0.5 (see Guidotti et al., 1994). Chemical analyses of chlorites with $Na_2O$+CaO+$K_2O$ contents >0.5 wt% were rejected and interpreted as contaminated.

3.4. Thermobarometric calculations

Empirical (Cathelineau, 1988; and Jowett, 1991) and semi-empirical (Inoue et al., 2009, 2018; Bourdelle et al., 2013; Bourdelle and Cathelineau, 2015; Lanari et al., 2014) thermometric methods were applied in chlorite. The structural site location of Ti, Mn, Na, Ca and K was done taking into account the configuration followed by each author.

The chlorite + white mica + quartz + $H_2O$ equilibrium was calculated in the KFMASH system using the software ChlMicaEqui (Lanari, 2012; Lanari et al., 2012). For these calculations, thermodynamic database of Berman (1988) was selected. This database contains modifications from Vidal et al. (2005, 2006) for chlorite, and Parra et al. (2002) and Dubacq et al. (2010) for white mica. For chlorite, the Vidal et al. (2005, 2006) solution model was selected, whereas the Parra et al. (2002) and Dubacq et al. (2010) models were selected for white mica. The Dubacq et al. (2010) model allowed calculating the equilibrium of chlorite-white mica incorporating the hydrated pyrophyllite end-member ($H_2O$ in A-site). In these equilibria, the $XFe^{3+}$ for chlorite and white mica were constrained from convergence methods of Vidal et al. (2005, 2006), which were consistent with those obtained from the approach of Inoue et al. (2018).

The chlorite + white mica + quartz + $H_2O$ equilibrium was modelled with the equilibria:

4 Daphnite +5 Mg-Amesite ←→ 4 Clinochlore + 5 Fe-Amesite (1)

14 alpha-Quartz + 5 Fe-Amesite + 3 Mg-Amesite + 8 $H_2O$ ←→ 4 Daphnite + 6 Sudoite (2)

15 alpha-Quartz + 10 Fe-Celadonite + 2 Mg-Amesite + Sudoite ←→ 10 Mg-Celadonite + 2 Daphnite + 4 Pyrophyllite (3)

75 alpha-Quartz + 2 Daphnite + 10 Muscovite + 5 Sudoite ←→ 2 Clinochlore + 10 Fe-Celadonite + 20 Pyrophyllite (4)

Clinochlore + 4 Daphnite + 5 Muscovite ←→ 5 Mg-Celadonite + 5 Fe-Amesite (5)

2 Fe-Amesite + 13 Mg-Amesite + 8 Muscovite + 14 Pyrophyllite + 30 $H_2O$ ←→ 8 Fe-Celadonite + 26 Sudoite (6)

The chlorite + hydrated white mica (WmH) + quartz + $H_2O$ equilibrium was modelled following the equilibria:

2 Phlogopite + 2 Pyrophyllite.$H_2O$ ←→ 2 Mg-Celadonite + 4 alpha-Quartz + Mg-Amesite (7)

26 alpha-Quartz + 5 Fe-Amesite + 2 Pyrophyllite.$H_2O$ ←→ 4 Daphnite - 8 Pyrophyllite (8)

4 Daphnite + 5 Mg-Amesite ←→ 4 Clinochlore + 5 Fe-Amesite (9)

14 alpha-Quartz + 5 Fe-Amesite + 3 Mg-Amesite + 8 $H_2O$ ←→ 4 Daphnite + 6 Sudoite (10)

15 alpha-Quartz + 10 Fe-Celadonite + 2 Mg-Amesite + Sudoite ←→ 10 Mg-Celadonite + 2 Daphnite + 4 Pyrophyllite (11)

75 alpha-Quartz + 2 Daphnite + 10 Muscovite + 5 Sudoite ←→ 2 Clinochlore + 10 Fe-Celadonite + 20 Pyrophyllite (12)

Clinochlore + 4 Daphnite + 5 Muscovite ←→ 5 Mg-Celadonite + 5 Fe-Amesite (13)

2 Fe-Amesite + 13 Mg-Amesite + 8 Muscovite + 14 Pyrophyllite + 30 $H_2O$ ←→ 8 Fe-Celadonite + 26 Sudoite (14)

The hydrated white mica + quartz + $H_2O$ equilibrium was calculated following the Dubacq et al. (2010) approach. This equilibrium is represented by a *P-T* line constructed from interlayer water content variation. Thus, a set of divariant *P-T* lines was obtained for each sample. For the calculation, an $XFe^{3+}$ of 0.5 was fixed in white mica (see Mineral chemistry method section). This equilibrium was modelled from:

Pyrophyllite.$H_2O$ ←→ Pyrophyllite + $H_2O$ (15)

3 Mg-Celadonite + 2 Pyrophyllite ←→ 11 alpha-Quartz + 2 Muscovite + Phlogopite + 2 $H_2O$ (16)

The uncertainties on the *P-T* calculations from the different thermobarometric methods applied in this work are approximately ±2 kbar and ±50º C (e.g., Vidal et al., 2006; Lanari et al., 2014).

## 4. Petrology of the metapelites

### 4.1. Mineral and structural relations

The metapelites from the Eastern and the Western belts in San Luis Formation (phyllites and minor slates) are characterized by high proportions of fine grained phyllosilicates (more than 50 wt%), phyllosilicate flakes with an average size of <100 μm, and scarce quartz-veins and detrital mineral phases. The mineral association contains white mica, chlorite, quartz, plagioclase and a low proportion of biotite, K-feldspar, calcite and

accessory minerals (rutile, apatite, zircon, tourmaline, pyrite, scarce ilmenite and monazite). The K-feldspar is only part of detrital mineral association, which is also composed of quartz ($Qz_1$), plagioclase ($Pl_1$) and a minor proportion of white mica ($Wm_1$) and biotite ($Bt_1$; partially replaced by chlorite). Graphite was recognized in black-metapelites (slates) and calcite ± iron oxides were locally observed in late quartz-veins.

In most samples, microstructures linked to $S_0$ and $S_1$ were identified (Fig. 4a-f), whereas an $S_2$ was also recognized locally (Fig. 4c, d, f). The $S_1$ is associated with $D_1$ linked to a $F_1$ folding stage, whereas $S_2$ is linked to $D_2$ stage that included a $F_2$ crenulation folding. The early compositional bedding ($S_0$) is represented by alternation of levels of <500 µm thick with significant variations of the modal proportion of phyllosilicates (white mica + chlorite ± biotite) and quartz-plagioclase (Fig. 4b). Detrital minerals are poorly preserved in quartz-plagioclase-rich beds, showing irregular to sub-rounded shapes, weak to moderate undulose extinction and sizes between 20 to 300 µm. Weak to moderate pressure-solution effects are identified in the contact between detrital $Qz_1$ grains. The $S_0$ is affected by a $D_1$ deformation stage and development of $S_1$ foliation (Fig. 4b). The $S_1$ is defined by inter-grown flakes (frequently 5 to 50 µm, up to 200 µm in coarser grain metapelites, Fig. 4e) of white mica ($Wm_2$), chlorite ($Chl_1$) and local occurrence of biotite ($Bt_2$) intercalated with elongated grains of quartz ($Qz_2$) and plagioclase/albite ($Pl_2$) (up to 100 µm long), defining continuous (Fig. 4a) to disjunctive foliation (phyllosilicate domains alternating with quartz microlithons, Fig. 4b). The $S_0$ and $S_1$ are deformed by the restricted $D_2$ stage and overprinted by the $S_2$ crenulation foliation. This second foliation is characterized by phyllosilicate domains (without quartz), which are intercalated with quartz-plagioclase-phyllosilicate microlithons, showing variable thickness, from a few microns up to 500 µm, anastomosed to parallel interrelationship and discrete to low-gradational contacts (Fig. 4c, d). The $S_2$ is defined by oriented white mica

($Wm_3$) and rarely chlorite ($Chl_2$) flakes (Fig. 4d, f), with grain-sizes from 10 to 50 µm (reaching up to 200 µm).

4.2. Clay minerals association

In the Western Belt the <2µm fraction is formed mainly by illite/K-white mica (22-89%), with variable proportions of interstratified I/S (0-33%), kaolinite (0-55%) and/or chlorite (0-24%), and goethite and quartz as subordinate phases (Fig. 5). In the Eastern Belt, illite/K-white mica appear with proportions similar to those in the Western Belt (20-91%), with I/S presence in most of the samples (0-29%). Kaolinite and chlorite proportions are different (0-1% and 0-65%, respectively), with one sample (FSL31039a1) reaching 83% of kaolinite. Table 1 shows the mineral associations obtained for each sample. In both belts, the interstratified I/S coexisting with white mica presents an R0 ordering type with <10% of white mica layers, except in a sample of the Western Belt (FSL-301013a1), in which R0, R1 and R3 ordering types were identified (Figs. 5b, d, e).

4.3. Chemical composition of the phyllosilicates

Average chemical analysis for chlorite and white mica from different textural positions are shown in Table 2 (full data is reported in the Supplementary Table 2). Chlorite is absent in sample FSL-31013a1.

The $Chl_1$ analyses obtained from the selected samples belonging to the Western Belt show Si values of 2.59±0.06 apfu (average ± standard deviation; values between 2.49 and 2.73 apfu), Al of 2.89±0.08 apfu (between 2.75 and 3.11 apfu) and XMg=Mg/($Fe_{Total}$+Mg) ($Fe_{Total}$ is all iron as $Fe^{2+}$) of 0.41±0.06 (between 0.31 and 0.49). Vacancies in the M1 site were calculated following Lanari et al. (2014), as ($A^{VI}$-$Al^{IV}$-Na-K)/2, obtaining mean contents of 0.03±0.04 apfu (all values <0.11 apfu). On the other hand, $Chl_1$ from the Eastern

Belt samples analysed contains 2.64±0.03 apfu of Si (between 2.57 and 2.76 apfu), 2.81±0.06 apfu of Al (between 2.66 and 2.92 apfu) and vacancies in the M1 site of 0.04±0.03 apfu, with values up to 0.11 apfu. The XMg values are 0.48±0.06 (between 0.37 and 0.62), with the highest values corresponding to a black slate sample (0.60-0.62; FSL-31037a), and the rest of the samples limited to the range of 0.37-0.52 (average of 0.47±0.05). The $Chl_2$ has been recognized in FSL-31032a sample, with Si contents of 2.64±0.04 apfu (between 2.58 and 2.75 apfu), Al contents of 2.78±0.05 apfu (between 2.65 and 2.84 apfu), XMg of 0.50±0.01 (between 0.49 and 0.52) and vacancies in the M1 site of 0.03±0.02 apfu (values up to 0.07 apfu). In both belts, chlorite analyses plot near or over the clinochlore-amesite segment in the chlorite compositional diagrams, $R^{2+}$ (Mg+Mn+$Fe_{Total}$) – Si (Fig. 6) (after Wiewióra and Weiss, 1990; modified by Bourdelle and Cathelineau, 2015) and there are no clear differences between the compositions of $Chl_1$ and $Chl_2$ (see Fig. 6b). However, when an initial $XFe^{3+}$ ratio is assumed (see methods section), the vacancies calculated as ($Al^{VI}$+$Fe^{3+}$-$Al^{IV}$-Na-K)/2 for $Chl_1$ show a mean value of 0.22±0.06 apfu (between 0.07 and 0.36 apfu) in the Western Belt and of 0.20±0.04 apfu (between 0.14 and 0.28 apfu) in the Eastern Belt, whereas for this last belt the $Chl_2$ presents an average value of 0.19±0.02 apfu (between 0.16 and 0.23 apfu). Thus, when $Fe^{3+}$ is taken into account the values show an increase in the sudoitic component, such as is shown in the $R^{2+}$-Si diagrams, when $R^{2+}$ is calculated with $Fe^{2+}$ instead of Fe total (see triangles in Fig. 6). In addition, the chemical composition of chlorite in each sample from Eastern and the Western belts are aligned to the Si + □ = $R_2^{2+}$ and $Si_{1.25}$ + $□_{0.75}$ = $R^{3+}$ + $R^{2+}$ substitution vectors (considering both the $Fe_{Total}$ as $Fe^{2+}$ and the $Fe^{2+}$ + $Fe^{3+}$), with apparent minor contribution of di-trioctahedral and tschermak substitutions (Fig. 6).

The $Wm_2$ analysed in the samples selected from the Western Belt has 3.11±0.05 apfu of Si (between 3.00 and 3.11 apfu), 2.68±0.11 apfu of Al (between 2.47 and 2.90 apfu) and

alkali content (Na+K) of 0.90±0.04 apfu (between 0.80 and 0.96 apfu). The XMg is constrained to 0.53±0.04 (between 0.42 and 0.60), except in FSL-31010a sample which exhibits lower XMg, with an average of 0.21±0.03 (from 0.16 to 0.26) (see Table 2). The $Wm_3$ was characterized in two samples, FSL-31013a1 and FSL-31016a, which contains Si of 3.16±0.03 apfu (from 3.10 to 3.22 apfu), Al of 2.59±0.04 apfu (from 2.52 to 2.68 apfu), alkalis of 0.90±0.04 apfu (from 0.79 to 0.94 apfu) and XMg of 0.55±0.03 (values between 0.49 and 0.61). The $Wm_3$ is more Si-richer than $Wm_2$ in FSL-31016a, although this behaviour is not observed in FSL-31013a1 (Fig. 7a,b). In the Eastern Belt, the $Wm_2$ has 3.17±0.07 apfu of Si (3.02-3.33 apfu), 2.59±0.13 apfu of Al (2.27-2.88 apfu) and alkalis of 0.89±0.04 (0.79-0.95 apfu). The XMg ratio has a value of 0.37±0.08 (0.20-0.54), except for FSL-31037a (black slate) with an average ratio of 0.66±0.05 (0.55-0.73). The $Wm_3$ was analyzed in the FSL-31032a sample, with Si contents of 3.22±0.05 apfu (3.14-3.29 apfu), Al of 2.47±0.09 apfu (values between 2.30 and 2.60 apfu), Na+K of 0.90±0.03 apfu (between 0.82-0.94 apfu) and XMg of 0.44±0.06 (0.32-0.52). In both belts, the white mica data show no clear differences between $Wm_2$ and $Wm_3$, as illustrated in Figure 7. For the Western Belt, the analyzes of $Wm_2$ and $Wm_3$ are apparently aligned with the pyrophyllitic vector, with a little influence of the tschermak substitution, and do not show a clear alignment with the ferrimuscovite and di/trioctahedral vectors (Fig. 7a, b). In white mica from the Eastern Belt, the effect of the tschermak substitution seems to be significant, with the exception of sample FSL-31034a3. This sample does not show a clear alignment with the tschermak substitution vector for white mica analyses (Fig. 7c, d).

## 5. Chrystallochemical indexes

5.1. Kübler Index ($KI_{CIS}$)

The $KI_{CIS}$ AD values were measured in the <2 μm fraction of 20 samples from both belts (Fig. 8a,b). In the Eastern Belt $KI_{CIS}$ values range from 0.19 to 0.26 Δº2θ (n: 10) with a mean value of 0.23 Δº2θ belonging to the epizone field (Table 1, Fig. 8a), with no significant modifications in the EG samples. In the Western Belt, obtained values range between 0.18 and 0.60 Δº2θ (n: 10), with a mean value of 0.30 Δº2θ belonging to the upper anchizone-epizone transition, with predominance of epizone values (Table 1, Fig. 8b). In two samples, $KI_{CIS}$ EG values (0.21-0.45 Δº2θ) are somewhat lower than $KI_{CIS}$ AD values (see Table 1, Fig. 8b), and together with the asymmetry of the white mica (001) reflections suggest the influence of small quantities of I/S (likely R3 ordering type). In general, values from the Western Belt are less homogeneous than the KI data from the Eastern Belt. $KI_{CIS}$ values corresponding to the 2-10 μm (Western Belt: mean ± standard deviation of 0.23±0.002 Δº2θ; Eastern Belt: 0.23±0.008 Δº2θ) and 10-20 μm (Western Belt: 0.21±0.012 Δº2θ; Eastern Belt: 0.21±0.010 Δº2θ) fractions measured in the 8 samples, also analysed by EMPA, are somewhat lower than the <2 μm fraction (Western Belt: 0.33± 0.183 Δº2θ; Eastern Belt: 0.25±0.010 Δº2θ; see Table 1 and Fig. 8a,b).

5.2. White mica *b* parameter

The white mica *b* parameter from the Eastern Belt gave a mean value of 9.014 Å (n: 11; 9.003 to 9.020 Å), while the Western Belt gave a mean value of 9.018 Å (n:9; 9.006 to 9.025 Å), without a clear trend along each transect. Both values are comparable with *b* parameter values of intermediate pressure facies series (inferred geothermal gradients of 25-35ºC/km) defined by Sassi and Scolari (1974) and Guidotti and Sassi (1986) (Fig. 9a). The white mica *b* parameters were calculated from chemistry mineral of white mica from samples analysed by EMPA (Table 2), using the formula proposed by Guidotti et al. (1989) [$b = 8.9931 + 0.0440\ \Sigma(Mg + Fe_{total})$]. The values obtained are between 9.013 to 9.026 Å for

the Eastern Belt (9.020 Å), and 9.013 to 9.023 Å (mean of 9.018 Å) for the Western Belt. In both cases, the ranges are comparable with those measured through XRD (Fig. 9a).

## 6. Thermobarometric calculations

### 6.1. Chlorite thermometry

Empirical and semi-empirical thermometry was applyed in all chlorite-bearing samples. The results of each sample with the average and standard deviation as 1 sigma (σ), are listed in Table 3. In general, empirical thermometry from Catherlineau (1988; abbreviates as C88) and Jowett (1991; abbreviates as J91) shows similar results in each sample. The average temperature for $Chl_1$ in the Western Belt ranges from 384º to 403º C (C88) and 389º to 413º C (J91), whereas in the Eastern Belt are: 349º C (C88) and 351º C (J91) in FSL-31037a, and 376º-379º C (C88) and 383º-384º C (J91) for FSL-31032a, FSL-31034a3 and FSL-31035a. In addition, the $Chl_2$ in the Eastern Belt (FSL-31032a) does not record significant differences with the $Chl_1$, with average values of 376º C (C88) and 381º C (J91) (see Table 3).

Two groups of semi-empirical thermometers were applied to chlorites: the first using Fe total as FeO (abbreviates as B13 for Bourdelle et al., 2013; and I18 for Inoue et al., 2018) and the last using Fe total as FeO + $Fe_2O_3$ (abbreviated as I09 for Inoue et al., 2009; and La14 for Lanari et al., 2014). The $Fe^{3+}/(Fe^{3+} + Fe^{2+})$ ratio was fixed such as it is explained in the analytical method descriptions. In addition, for the Lanari et al. (2014) thermometer the Si content in chlorite must not exceed 3 apfu, whereas up to 4 apfu is accepted for the Inoue et al. (2009, 2018) and Bourdelle et al. (2013) thermometers. For the last thermometers, where Fe total is FeO, the value of vacancies should be >0.05 apfu, being defined as $(Al^{VI}-Al^{IV}-Na-K)/2$ (cf. Lanari et al., 2014). On the other hand, when $Fe^{3+}$ is estimated, the vacancies were calculated as $6-(Fe^{2+}+Fe^{3+}+Mg+Al^{VI})$ for Inoue et al. (2009) and as $(Al^{VI}-Al^{IV}+Fe3^{+}-Na-K)/2$

for Lanari et al. (2014). The thermometer of Bourdelle et al. (2013) was applied only in few analyses since most of them do not reach the minimum vacancy criteria for this calibration, with the exception of the FSL-31034a3 sample (see Fig. 6 and Table 3). However, temperatures obtained with B13 are similar to the rest of the applied thermometers (see Table 3). In the Western Belt, temperature averages for $Chl_1$ range between 351º-367º C (I18), 364º-386º C (I09) and 380º-416º C (La14), whereas in the Eastern Belt they are between 283º-349º C (I18), 301º-367º C (I09) and 352º-403º C (La14). The $Chl_2$ in FSL-31032a records mean temperatures of 348º (I18), 364º C (I09) and 398º C (La14), being similar to those from $Chl_1$ in the same sample (Table 3).

6.2. Multi-equilibrium thermobarometry

The *P-T* conditions from the local equilibrium of chlorite ($Chl_1$) - white mica ($Wm_2$) pairs were calculated using the chlorite + white mica + quartz + $H_2O$ equilibrium and are summarized in Table 4 and Figure 10. These calculations were made for $Chl_1$-$Wm_2$ pairs in FSL-31009a2 and FSL-31016a samples from the Westen Belt (see Fig. 4e), and FSL-31032a and FSL-31034a3 samples from the Easten Belt (see Fig. 4f). The *P-T* conditions were constrained in 317º C and 5.1 kbar for FSL-31009a2 (Fig. 10a) and 365-480 ºC – 2.5-4.6 kbar for FSL-31016a (Fig. 10b,c). In the Eastern Belt, the FSL-31034a3 sample records 401-408 ºC and 4.3-4.7 kbar (Fig. 10d), whereas in the FSL-31032a sample, values are of 361-380 ºC and 3.3-3.6 kbar (Fig. 10e,f). In addition, two $Chl_2$-$Wm_3$ pairs from the FSL-31032a sample were analyzed, obtaining values of 433º C-3.2 kbar and 442º C-2.8 kbar. In the FSL-31032a, the $XFe^{3+}$ of $Chl_1$ and $Chl_2$ were adjusted to >0.15 to achieve the equilibrium. $XFe^{3+}$ values higher than 0.15 are consistent with those obtained from Inoue et al. (2018) for this sample ($XFe^{3+}$ = 0.20, see Table 2).

The hydrated white mica + chlorite + quartz + $H_2O$ equilibrium was calculated for $Chl_1$-$Wm_2$ pairs (Table 4). In the Western Belt, *P-T* conditions of 359º C and 8.9 kbar were calculated in FSL-31009a2, whereas 375º C and 4.9 kbar were obtained for FSL-310016a. In the Eastern Belt, 354º C and 3.4 kbar were calculated for the FSL-31032a sample. On the other hand, the equilibrium of hydrated white mica + quartz + $H_2O$ from Dubacq et al. (2010), considering the pressures calculated from the white mica + chlorite + quartz + $H_2O$ equilibrium, was calculated for both belts. At around 5 kbar, the temperatures estimated for the Western Belt are of 340-420º C in FSL-31009a2, 340-420º in FSL-31013a1, and 370-430º C in the FSL-31016a. In the Eastern Belt, the temperature in FSL-31034a3 was estimated in the range of 330-420º C at 4.5 kbar, 310-390º C in FSL-31035a at 4.5 kbar, whereas in FSL-31032a is 285-370º C at 3.5 kbar. In addition, the temperature for $Wm_3$ in FSL-310032a was estimated in 300-370º C at 3 kbar (see Table 4 and Fig. 10g,h).

## 7. Discussion

### 7.1. Analysis of crystallochemical indexes

The $KI_{CIS}$ values (<2μm) obtained for both belts are generally found in the epizone field and there are no significant differences between samples that recorded more than one growth episode of white mica (Wm2, Wm3). For the Eastern Belt, the values are all in this field and do not present any tendency (Fig. 8a), whereas for the Western Belt there is a slight increase in the $KI_{CIS}$ values (anquizone field) towards the west (see Fig. 8b), with one sample presenting diagenetic values.

In addition to the <2μm fraction, the $KI_{CIS}$ was measured in the 2-10 μm and 10-20 μm fractions corresponding to the 8 samples also studied by EMPA, mainly because the <2μm fraction does not include the size of the petrographically identified of $Wm_2$ and $Wm_3$ (both, associated with $S_1$ and $S_2$, exceeding 5 μm), but also to assess the influence of the grain

size on this indicator. Although the problems related to the influence of the granulometric fraction on which the KI measurement is made have been mentioned several times (Kübler and Jaboyedoff, 2000; Jaboyedoff et al., 2001; Kisch et al., 2004), these have been fundamentally linked to the presence of detrital white mica, very common in diagenetic and anquizonal samples (Kübler and Jaboyedoff, 2000). In the case of the epizonal samples, and as it has been seen in the samples of this work, the <2μm fraction is in general substantially lower than the grain size of the neoformed white micas. Thus, the <2μm fraction do not include most of the material formed during the prograde and, at the same time this fine fraction could contain grains associated with processes subsequent to the metamorphic peak (e.g., retrograde diagenesis, Nieto et al., 2005, processes associated with decompression, Muñoz et al., 2017). It should be noted that, although KI is a very sensitive indicator from the diagenesis to the epizone in different geotectonic contexts, and is widely used to characterize the low grade metamorphism (equivalent to the low greenschist facies; Jaboyedoff, 2001), it is a specific index of anquizone (Abad, 2007) and its sensitivity decreases as we move away from this field toward diagenesis or epizone. In the case of the San Luis Formation, although most of the values are restricted to the epizone field, the different granulometric fractions analyzed show a tendency with higher values towards the finer fractions (Fig. 8c). For the 10-20 μm fraction (which concentrates the white micas on which the mineral chemistry measurements were made), $KI_{(CIS)}$ values between 0.20-0.23 °Δ2θ were obtained, which would be associated with temperatures higher than 300ºC (which is the temperature estimated for the transition between anchizone and epizone fields, see Merriman and Frey, 1999). It should be noted that the samples FSL-31008a1 and 31008a2 have anchizonal values and sample FSL 31013a1 diagenetic values for the <2 μm fraction. In the case of the sample FSL-31013a1 this value is substantially higher than those obtained for the 2-10 (0.24 °Δ2θ) and 10-20 μm fractions (0.21 °Δ2θ) (see table 1). These higher values could be associated with

processes that would have taken place after the two main growth episodes, at lower temperature conditions, as indicated by the presence of I/S and/or kaolinite in the <2μm fraction of most of the analyzed samples, with mineral associations that suggest an episode of mineral growth in diagenetic conditions (<200º C; Merriman and Frey, 1999).

The cumulative frequency curves of white mica *b* parameter values obtained from the XRD measurements are similar to those from New Hampshire and Ryoke Belt (Fig. 9a), and indicate that the two belts were metamorphosed under intermediate pressure facies conditions (Guidotti and Sassi, 1986, Fig. 9a), suggesting intermediate thermal gradients of 25-35 ºC/km (Merriman and Peacor, 1999). These values are similar to those obtained from the chemical analyses (see Table 2), where the *P-T* conditions calculated for $Wm_2$-$Chl_1$, associated to $D_1$-$S_1$, are consistent with the range of *b* parameter values as shown in Figure 9b. The selected samples from both belts are projected in the *P-T* diagram proposed by Guidotti and Sassi (1986), which included isopleths for the white mica *b* parameter values. Thus, pressure values ranging from 2.7 to 3.9 kbar are obtained from the combination of semi-empirical chlorite thermometry average temperatures (Inoue et al., 2009, 2018; Lanari et al., 2014) and the white mica *b* parameter values measured in each sample.

7.2. Thermobarometric results

Empirical and semi-empirical chlorite thermometers show similar results in each sample for $Chl_1$ ($S_1$) (Table 3). Thus, considering all the samples, mean temperatures for chlorite empirical thermometers are constrained between 384-413º C in the Western Belt and 349-384º C in the Eastern Belt. Temperatures for chlorite semi-empirical thermometers are between 316-416º C in the Western Belt and 261-403º C in the Eastern Belt, suggesting a consistency between both methods in each sample (Table 3). These values show a trend to lower temperatures in Bourdelle et al. (2013) and Inoue et al. (2018) semi-empirical

calibrations, which consider the Fe Total as FeO. Within the semi-empirical methods that included the $Fe^{3+}$, the thermometer proposed by Lanari et al. (2014; La14) systematically yields temperatures higher than those from Inoue et al. (2009), as it was previously observed by Vidal et al. (2016). On the other hand, the Dubacq et al. (2010) method shows results similar to previous thermometers, thus 340-430º C are obtained in the Western Belt, and 285-420º C in the Eastern Belt. The thermobarometric results from chlorite ($Chl_1$) - white mica ($Wm_2$) - quartz - $H_2O$ equilibrium show temperatures between 317-480º C and 2.5-5.1 kbar in the Western Belt and 362-408º C and 3.3-4.7 kbar in the Eastern Belt (Table 4). When hydrated white mica is included in this equilibrium, the *P-T* conditions are comparable (Table 4). Spatially, significant variations in temperatures for $Chl_1$, for all methods, are not observed in the Western Belt. On the other hand, the Eastern Belt shows variations in temperatures, but without clear temperature field gradient, being the lowest temperature recorded in a black-slate sample (FSL-31037a).

Similar empirical and semi-empirical chlorite temperatures are obtained between $Chl_1$ (349-403º C) and $Chl_2$ (343-398º C) in the FSL-31032a sample (Table 3). These suggest that $Chl_2$ ($D_2$-$S_2$) formed close to the temperature peak of $Chl_1$, which is consistent with similar compositions between $Wm_2$ and $Wm_3$ in this sample. However, the chlorite – white mica – quartz – $H_2O$ equilibrium results show slightly higher temperatures and lower pressures for $Chl_2$ (Tabla 4). However, the possibility of a chemical $Chl_1$-$Wm_2$ re-equilibrium during the $Chl_2$-$Wm_3$ growth episode, without obvious textural modification (e.g., Scheffer et al., 2016; Airaghi et al., 2017) should be not discarded.

Pressure values calculated from white mica – chlorite pairs are quite similar in most calculation for both belts (Table 4). However, a value of 8.9 kbar calculated from chlorite – white mica (hydrated) – quartz – $H_2O$ equilibrium for FSL-31009a2 is not consistent with the rest of the calculations, unlike temperature (Table 4). This pressure value contrasts, and

seems unrealistic, with respect to values estimated in previous works for the San Luis Formation and nearby schists of Sierra de San Luis. Ortiz Suárez and Casquet (2005) and Morosini and Ortiz Suárez (2011) obtained values between 4-6 kbar, similar to those obtained in this work (2.5-5.1 kbar, Table 4).

**Final comments and conclusions**

Results obtained in this work for the San Luis Formation show the advantages of the multiproxy study, showing a very good consistency between the methods of thermobarometric calculations and crystallochemical indexes to estimate the *P-T* conditions in low-grade metamorphic units. Crystallochemical indexes are ideal to characterize units distributed across wide regions. A dense and systematic sampling allows identifying mineralogical changes in an expeditious way (e.g., prograde, retrograde, metasomatic effects, variations in the compositions of the protoliths; Collo et al., 2008; Potel et al., 2016; Vazquez et al., 2016) and *P-T* variations (e.g., field gradients, structural effects), which makes it possible to generate a basic characterization in which subsequent quantitative studies are based. Moreover, the use of empirical and semi-empirical chlorite thermometers and the multiequilibrium methods allow making a precise constrain of *P-T* conditions, including comparisons between different calibrations as well as estimation of the $XFe^{3+}$ in chlorite. The $XFe^{3+}$ estimated from comparison of temperatures calculated with different thermometers (Fe total as FeO and Fe Total as $FeO + Fe_2O_3$) are similar to those calculated from convergence methods in the chlorite – white mica – quartz – $H_2O$ equilibrium (see Tables 2 and 4). The themobarometric methods also allows identifying *P-T* conditions variation related to compositional zoning (e.g., Lanari et al., 2012) and partial re-equilibration (e.g., Airaghi et al., 2017). This is a strong advantage in comparison to the crystallochemical indexes which do not allow identifying local compositional variations.

Comparable temperatures were obtained from KI measurements, which allow inferring temperatures >300°C (epizone conditions), and from those from chlorite thermometers (261-416º C) and chlorite - white mica – quartz – $H_2O$ equilibrium (317-480º C). Pressure conditions inferred from the white mica *b* parameter are also consistent with the pressures calculated from the white mica-chlorite equilibrium pair as shown in Fig. 9b. Moreover, the similarity between the *b* parameter values measured through XRD and those calculated from the mineral chemistry reinforce the reliability in these crystallochemical indexes.

A retrograde process was identified based on the mineralogy of the <2 μm, which presents I/S and Kln, and in three KI values compatible with anchizonal and diagenetic conditions. This reinforces the approach of using not only the <2μm fraction but larger grains size fractions for the KI measurement in low-grade metamorphic rocks, where the newly formed mineral phases could have substantially larger sizes. The measurement of the KI and the mineralogical characterization by means of XRD in several granulometric fractions, including the mean grain size defined petrographically for the white micas associated with the main foliation, would guarantee the identification and elimination of the influence of retrograde phases that could potentially mask the conditions of the prograde metamorphism.

**Acknowledgements**

Financial support for this paper was provided by Argentine public grants CONICET 2015-11220150100901CO, FONCYT PICT 2013-0472, SECyT 2016-30720150100830CB and PUE-2016-CONICET. The authors thank Drs. Pierre Lanari and Isabel Abad for the observations and recommendation, which have substantially improved this work. Also, we are very grateful to Dr. Fernando Colombo, Dr. Fernando Nieto and Dr. Benoit Dubacq for their help with the work.

**References**

Abad, I., 2007. Physical meaning and applications of the illite Kübler index: measuring reaction progress in low-grade metamorphism. In: Nieto F., Jiménez-Millán J., (Eds.), Diagenesis and Low-Temperature Metamorphism. Theory, Methods and Regional Aspects. Seminarios de la Sociedad Española de Mineralogía. Volumen 3, Sociedad Española de Mineralogía, Jaén, 53-64.

Abad, I., Nieto, F., Gutiérrez-Alonso, G., Do Campo, M., López-Munguira, A., Velilla, N., 2006. Illitic substitution in micas of very low-grade metamorphic clastic rocks. European Journal of Mineralogy 18, 59-69.

Airaghi, L., Lanari, P., de Sigoyer, J., Guillot, S., 2017. Microstructural vs compositional preservation and pseudomorphic replacement of muscovite in deformed metapelites from the Longmen Shan (Sichuan, China). Lithos, 282-283, 262-280.

Árkai, P., 1991. Chlorite crystallinity: an empirical approach and correlation with illite crystallinity, coal rank and mineral facies as exemplified by Palaeozoic and Mesozoic rocks of northeast Hungary. Journal of Metamorphic Geology 9, 723-734.

Berman, R.G., 1988. Internally-consistent thermodynamic data for minerals in the system $Na_2O$-$K_2O$-CaO-MgO-FeO-$Fe_2O_3$-$A1_2O_3$-$SiO_2$-$TiO_2$-$H_2O$-$CO_2$. Journal of Petrology 29, 445-522.

Bourdelle, F., Cathelineau, M., 2015. Low-temperature chlorite geothermometry: a graphical representation based on a T–$R^{2+}$–Si diagram. European Journal of Mineralogy 27, 617–626.

Bourdelle, F., Parra, T., Chopin, C., Beyssac, O., 2013. A new chlorite geothermometer for diagenetic to low grade metamorphic conditions. Contributions to Mineralogy and Petrology 165, 723–735.

Cantarero, I., Lanari, P., Vidal, O., Alías, G., Travé, A., Baqués, V., 2014. Long-term fluid circulation in extensional faults in the central Catalan Coastal Ranges: P-T constraints from neoformed chlorite and K-white mica. International Journal of Earth Sciences, 103, 165-188.

Cathelineau M., 1988. Cation site occupancy in chlorites and illites as function of temperature. Clay Minerals 23, 471–485.

Cathelineau, M., Nieva, D., 1985. A chlorite solid solution geothermometer the Los Azufres (Mexico) geothermal system. Contributions to Mineralogy and Petrology 91, 235–244.

Collo, G., Astini, R.A., Cardona, A., Do Campo, M.D., Cordani, U., 2008. Edad del metamorfismo de las unidades con bajo grado de la regio´n central del Famatina: La impronta del ciclo orogénico oclóyico. Revista Geológica de Chile, 35, 191–213.

Delpino, S., Rueda, M., Urraza, I., Grasemann, B., 2015. Microstructural development in ductile deformed metapelitic-metapsamitic rocks: A case study from the greenschist to granulite facies megashear zone of the Pringles Metamorphic Complex, Argentina. In: Mukherjee, S., Mulchrone, K.F. (Eds.), Ductile Shear Zones: From Micro- to Macro-scales, Wiley-Blackwell, Chichester, 224-249.

Drobe, M., López de Luchi, M.G., Steenken, A., Frei, R., Naumann, R., Siegesmund, S., Wemmer, K., 2009. Provenance of the late Proterozoic to early Cambrian metaclastic sediments of the Sierra de San Luis (Eastern Sierras Pampeanas) and Cordillera Oriental, Argentina. Journal of South American Earth Science 28, 239–262.

Dubacq, B., Vidal, O., de Andrade, V., 2010. Dehydration of dioctahedral aluminous phyllosilicates: Thermodynamic modelling and implications for thermobarometric estimates. Contributions to Mineralogy and Petrology 159 (2), 159-174.

González, P.D., Sato, A., Llambías, E., Basei, M., Vlach, S., 2004. Early Paleozoic structural and metamorphic evolution of western Sierra de San Luis (Argentina), in relation to Cuyania accretion. Gondwana Research 7, 1157–1170.

Guidotti, C., Sassi, F., 1986. Classification and correlation of metamorphic facies series by means of muscovite $b_0$ data from Low-grade metapelites. Neues Jahrbuch fur Mineralogie Abhandlungen 157, 363–380.

Guidotti, C., Sassi, F., Blencoe, J., 1989. Compositional controls on the a and b cell dimensions of $2M_1$ muscovite. European Journal of Mineralogy 1, 71–84.

Guidotti, C.V., Yates, M.G., Dyar, M.D., Taylor, M.E., 1994. Petrogenetic implications of the $Fe^{3+}$ content of muscovite in pelitic schists. American Mineralogist 79, 793–795.

Hauzenberger, Ch.A., Mogessie, A., Hoinkes, G., Felfernig, A., Bjerg, E.A., Kostadinoff, J., Delpino, S., Dimieri, L., 2001. Metamorphic evolution of the Sierras de San Luis: Granulite facies metamorphism related to mafic intrusions. Mineralogy and Petrology 71, 95–126.

Hillier, S., Velde, B., 1991. Octahedral occupancy and chemical composition of diagenetic (low-temperature) chlorites. Clay Minerals 26, 149–168.

Inoue, A., Meunier, A., Patrier-Mas, P., Rigault, C., Beaufort, D., Vieillard, P., 2009. Application of chemical geothermometry to low-temperature trioctahedral chlorites. Clays and Clay Minerals 57, 371–382.

Inoue, A., Inoué, S., Utada, M., 2018. Application of chlorite thermometry to estimation of formation temperature and redox conditions. Clay Minerals, in press., 1-37. DOI: 10.1180/clm.2018.10.

Jaboyedoff, M., Bussy, F., Kübler, B., Thelin, Ph., 2001. Illite "crystallinity" revisited. Clays and Clay Minerals 49, 156-167.

Jowett, E., 1991. Fitting iron and magnesium into the hydrothermal chlorite geothermometer. Program Abstract 16, A62.

Kisch, H.J., Árkai, P., Brime, C., 2004. On the calibration of the illite Kübler index (illite "crystallinity"). Schweizerische Mineralogische und Petrographische Mitteilungen 84 (3), 323-331.

Kübler, B., 1964. Les argiles, indicateurs de métamorphisme. Revue de l'Institute Francais du Petrolé 19, 1093–1112.

Kübler, B., Jaboyedoff, M., 2000. Illite crystallinity. Comptes Rendus de l'Academie de Sciences - Serie IIa: Sciences de la Terre et des Planetes 331, 75-89.

Lanari, P., 2012. Micro-cartographie P–T–□ dans les roches métamorphiques Applications aux Alpes et à l'Himalaya. Earth Sciences. PhD-Thesis, Université de Grenoble, French, pp. 544.

Lanari, P., Engi, M., 2017. Local bulk composition effects on metamorphic mineral assemblages. Reviews in Mineralogy and Geochemistry 83, 55-102.

Lanari, P., Guillot, S., Schwartz, S., Vidal, O., Tricart, P., Riel, N., Beyssac, O., 2012. Diachronous evolution of the alpine continental wedge: evidences from P–T estimates in the Briançonnais Zone houillère (France-Western Alps). Journal of Geodynamics 56-57, 39–54.

Lanari, P., Wagner, T., Vidal, O., 2014. A thermodynamic model for di-trioctahedral chlorite from experimental and natural data in the system $MgO–FeO–Al_2O_3–SiO_2–H_2O$: applications to P–T sections and geothermometry. Contributions to Mineralogy and Petrology 167, 1–19.

Merriman, R.J., Frey, M., 1999. Patterns of very low-grade metamorphism in metapelitic rocks. In: Frey, M., Robinson, D., (Eds.), Low-Grade Metamorphism. Blackwell Science, 61-107.

Merriman, R.J., Peacor, D.R., 1999. Very low grade metapelites: Mineralogy, microfabrics and measuring reaction progress. In: Frey, M., Robinson, D., (Eds.), Low-Grade Metamorphism. Blackwell Science, 10-60.

Moore, D.M., Reynolds, R.C., 1997. X-Ray diffraction and the identification and analysis of clay minerals. Oxford University Press, 378 pp.

Morosini, A., Ortiz Suárez, A., 2011. Contact metamorphism of the La Escalerilla Granite, in the area La Carolina, San Luis. Revista de la Asociacion Geologica Argentina 68 (2), 277-289.

Morosini, A.F., Ortiz Suárez, A.E., Otamendi, J.E., Pagano, D.S., Ramos, G.A., 2017. La Escalerilla pluton, San Luis Argentina: The orogenic and post-orogenic magmatic evolution of the famatinian cycle at Sierras de San Luis. Journal of South American Earth Sciences 73, 100-118.

Muñoz, F., Collo, G., Verdecchia, S.O., Palape, C., 2017. Caracterización metamórfica de unidades metapelíticas de la Serie Occidental de La Cordillera de la Costa: el afloramiento de Infiernillo, Pichilemu, Chile. In: Ibañez L., Grosse P., Báez M. (Eds.), XX Congreso Geológico Argentino, Acta del Sesión Técnica 5: Petrología de rocas Metamórficas. Facultad de Ciencias Naturales e Instituto Miguel Lillo, Universidad Nacional de Tucumán, San Miguel de Tucumán (Argentina). 56-58.

Nieto, F., Mata, P.M., Bauluz, B., Giorgetti, G., Árkai, P., Peacor, D.R., 2005. Retrograde diagenesis, a widespread process on a regional scale. Clay Minerals 40, 93-104.

Ortiz Suárez, A., Casquet, M.C., 2005. Inversión metamórfica en el orógeno famatiniano de la Sierra de San Luis, Argentina. Geogaceta 38, 231-234.

Parra, T., Vidal, O., Agard, P., 2002. A thermodynamic model for Fe–Mg dioctahedral K white micas using data from phase-equilibrium experiments and natural pelitic assemblages. Contribution to Mineralogy and Petrology 143, 706–732.

Pattison, D.R.M., 1992. Stability of andalusite and sillimanite and the $Al_2SiO_5$ triple point: Constraints from the Ballachulish aureole, Scotland. Journal of Geology 100, 423–446.

Perón Orrillo, J.M., Rivarola, D., 2014. Descripción litofacial e interpretación genética de los metaconglomerados de la Formación San Luis (Proterozoico superior - Cámbrico), sierra de San Luis, Argentina. Latin American Journal of Sedimentology and Basin Analysis 21 (1), 25–48.

Potel, S., Maison, T., Maillet, M., Sarr, A., Patrick Doublier, M., Trullenque, G., Ferreiro Mählmann, R., 2016. Reliability of very low-grade metamorphic methods to decipher basin evolution: Case study from the Markstein basin (Southern Vosges, NE France). Applied Clay Science 134, 175–185.

Powell, R., Holland, T.J.B., 2008. On thermobarometry. Journal of Metamorphic Geology, 26, 155–179.

Prozzi, C.R., 1990. Consideraciones acerca del basamento de San Luis, Argentina. XI Congreso Geológico Argentino, 452-455.

Rapela, C.W., Verdecchia, S.O., Casquet, C., Pankhurst, R.J., Baldo, E.G., Galindo, C., Murra, J.A., Dahlquist, J.A., Fanning, C.M., 2016. Identifying Laurentian and SW Gondwana sources in the Neoproterozoic to Early Paleozoic metasedimentary rocks of the Sierras Pampeanas: Paleogeographic and tectonic implications. Gondwana Research 32, 193–212.

Reynolds, R.C., 1985. NEWMOD©, a Computer Program for the Calculation of One-Dimensional Diffraction Patterns of Mixed-Layered Clays. R.C. Reynolds, Jr., 8 Brook Road, Hanover, New Hampshire 03755, U.S.A.

Sassi, F., Scolari, A., 1974. The $b_0$ of the potassic white micas as a barometric indicator in low-grade metamorphism of pelitic schist. Contributions to Mineralogy and Petrology 45: 143-152.

Siegesmund, S., Steenken, A., Martino, R., Wemmer, K., López de Luchi, M.G., Frei, R., Presnyakow, S., Guerschi, A., 2010. Time constraints on the tectonic evolution of the Eastern Sierras Pampeanas (Central Argentina). International Journal of Earth Sciences 99, 1199–1226.

Scheffer, C., Vanderhaeghe, O., Lanari, P., Tarantola, A., Ponthus, L., Photiades, A. France, L., 2016. Syn- to post-orogenic exhumation of metamorphic nappes: Structure and thermobarometry of the western Attic-Cycladic metamorphic complex (Lavrion, Greece). Journal of Geodynamics, 96, 174-193.

Steenken, A., Siegesmund, S., López de Luqui, M.G., Frei, R., Wemmer, K., 2006. Neoproterozoic to Early Palaeozoic events in the Sierra de San Luis: implications for the Famatinian geodynamics in the Eastern Sierras Pampeanas (Argentina). Journal of Geological Society of London 163, 965–982.

Steenken, A., Siegesmund, S., Wemmer, K., López de Luchi, M.G., 2008. Time constraints on the Famatinian and Achalian structural evolution of the basement of the Sierra de San Luis (Eastern Sierras Pampeanas, Argentina). Journal of South American Earth Science 25, 336–358.

Stüwe, K., 1997. Effective bulk composition changes due to cooling: a model predicting complexities in retrograde reaction textures. Contributions to Mineralogy and Petrology 129, 43–52.

Trincal, V., Lanari, P., 2016. Evidence of Al-free di-trioctahedral substitution in chlorite and a ferri-sudoite end-member. Clay Minerals 51, 675-689.

Vazquez, M., Bauluz, B., Nieto, F., Morata, D., 2016. Illitization sequence controlled by temperature in volcanic geothermal systems: The Tinguiririca geothermal field, Andean Cordillera, Central Chile. Applied Clay Science 134, 221-234.

Vidal, O., Parra, T., Trotet, F., 2001. A thermodynamic model for Fe–Mg aluminous chlorite using data from phase equilibrium experiments and natural pelitic assemblages in the 100 to 600 C, 1 to 25 kbar range. American Journal of Science 301, 557–592.

Vidal, O., Parra, T., Vieillard, P., 2005. Thermodynamic properties of the Tschermak solid solution in Fe-chlorite: application to natural examples and possible role of oxidation. American Mineralogist 90, 347–358.

Vidal, O., de Andrade, V., Lewin, E., Muñoz, M., Parra, T., Pascarelli. S., 2006. P-T-deformation-Fe3+/Fe2+mapping at the thin section scale and comparison with XANES mapping: application to a garnet-bearing metapelite from the Sambagawa metamorphic belt (Japan). Journal of Metamorphic Geology 24, 669–683.

Vidal, O., Lanari, P., Munoz, M., Bourdelle, F., de Andrade, V., 2016. Temperature, pressure, oxygen-activity conditions of chlorite formation. Clay Minerals 51, 615-633.

von Gosen, W., 1998. The Phyllite and Micaschist Group with associated intrusions in the Sierra de San Luis (Sierras Pampeanas/Argentina)-structural and metamorphic relations. Journal of South American Earth Sciences 11, 79-109.

von Gosen, W., Prozzi, C., 1998. Structural Evolution of the Sierra de San Luis (Eastern Sierras Pampeanas, Argentina): implications for the proto-andean Margin of Gondwana. In: Pankhurst, R.J., Rapela, C.W. (Eds.), The Proto-Andean Margin of Gondwana 142. Geological Society, London, 235-258.

Warr, L.N., Ferreiro Mählmann, R., 2015. Recommendations for Kübler Index standardization. Clay Minerals 50, 283-286.

Warr, L.N., Rice, A.H.N., 1994. Interlaboratory standardization and calibration of day mineral crystallinity and crystallite size data. Journal of Metamorphic Geology 12 (2), 141-152.

Wiewiora, A., Weiss, Z., 1990. Crystallochemical classifications of phyllosilicates based on the unified system of projection of chemical composition: II The chlorite group. Clay Minerals 25, 83–92.

Wemmer, K., Steenken, A., Müller, S., López de Luchi, M.G., Siegesmund, S., 2011. The tectonic significance of K/Arillite fine-fraction ages from the San Luis Formation (Eastern Sierras Pampeanas, Argentina). International Journal of Earth Sciences, Geologiche Rundschau 100, 659–669.

Whitney, D.L., Evans, B.W., 2010. Abbreviations for names of rock-forming minerals. American Mineralogist 95, 185-187.

Yavuz, F., Kumral, M., Karakaya, N., Karakaya, M.T., Yildirim, D.K., 2015. A Windows program for chlorite calculation and classification. Computers and Geosciences 81, 101-113.

**Figure captions**

Fig. 1. (a) Geological map of the Northwestern Argentine with the location of the study area, modified from Rapela et al. (2016). Location of the Sierra de San Luis for Fig. 1b is shown in a grey square. (b): Detail of the geology of the Sierra de San Luis, included both the Eastern and the Western belts studied in this work. The location of figures 2a and 2b is also shown. Abbreviations: San Salvador del Jujuy (Ju), Salta (Sal), Tucumán (Tuc), La Rioja (LR), San Juan (SJ), Mendoza (Mz), San Luis (SL), Catamarca (Ca) and Córdoba (Cba).

Fig. 2. Detail of the Western (a) and Eastern (b) belts in which the sampling point and the methodologies applied to each sample are indicated.

Fig. 3. Outcrop view of the studied sequences showing the centimetric (a, b) alternance of metapelitic (shale) and metapsammitic (silty-sandy) layers associated with the $S_0$ primary foliation. The $S_1$ foliation is parallel (a) to subparallel with $S_0$ (b and c). Figures a and b from the Western Belt, and c from the Eastern Belt.

Fig. 4. Microphotographs of the phyllites from the San Luis Formation. (a) Metapelite showing the development of the main $S_1$ foliation, which is represented by aligned $Wm_2$ and $Chl_1$. (b) Relation between $S_0$ and $S_1$ in microfolding ($F_1$) hinge area affecting the alternation of quartz-plagioclase-rich and phyllosilicate-rich layers. (c, d) Crenulation cleavage ($S_2$) affecting the $S_1$ ($Wm_2$+$Chl_1$) and represented by aligned sheets of $Wm_3$ (c; FSL-31016a sample) or $Wm_3$ – $Chl_2$ (d; FSL-31032a sample). (e) and (f) are backscattered electron imaging obtained from electron microprobe that show details of mineral assemblage in (c) and (d) respectively. In both images, point analysis for chlorite-white mica pairs used for thermobarometry are indicated as yellow (chlorite) and orange (white mica) triangles. Number of each analysis is described in each point.

Fig. 5. X-ray diffraction diagrams comparing air dried (AD), glycolated (EG) and calcinated oriented (HO) samples (a, b and c: samples from Western belt; d and e: samples from Eastern belt).

Fig. 6. Chemical composition diagrams of chlorites, $Chl_1$ ($S_1$) and $Chl_2$ ($S_2$), from the Western (a) and the Eastern belts (b) (after Wiewióra and Weiss, 1990, modified by Bourdelle and Cathelineau, 2015). The triangles represent the composition of chlorites with $Fe^{3+}$ in the calculation (Fe total as $Fe^{2+}$ + $Fe^{3+}$), preserving the color of the symbol (circle) for each sample. See text for descriptions.

Fig. 7. Diagrams showing chemical compositions of white micas, $Wm_2$ ($S_1$) and $Wm_3$ ($S_2$), in Western (a, b) and Eastern (c, d) belts. Arrows represent different exchange vectors (modified from Abad et al., 2006): $Al^{VI} = Fe^{3+}$ (ferrimuscovite), $\square^{VI} + (Al^{IV}, Al^{VI}) = 3R^{2+}$ (di/trioctahedral), $Al^{IV} + Al^{VI} = Si + R^{2+}$ (Tschermak), $Al^{IV} + (Na, K)^{A} = Si + \square^{A}$ (pyrophyllite).

Fig. 8: Kübler index value ($KI_{CIS}$) distribution along the belts obtained by air dried (AD) and glycolated (EG) methods. (a) and (b) are values for the <2μm fraction from the Eastern and the Western belts, respectively. (c) Set of values for the <2μm, 2-10 μm and 10-20 μm fractions in samples that also were analysed through electron microprobe. Temperatures according to Merriman and Peacor (1999).

Fig. 9. (a) Cumulative frequency curves for the white mica *b* parameter values from both belts. These curves were projected from *b* parameter values measured with XRD and calculated from mineral chemistry (average in each sample, see Table 2). As reference low-pressure, intermediate-pressure, and high-pressure fields from Guidotti and Sassi (1986) are shown, and curves from other well-characterized low-grade metamorphic terranes are added (cf. Sassi and Scolari, 1974). (b) *P-T* diagram shows *b*-parameter isopleths (after Guidotti and Sassi, 1986) and theorical curves for kaolinite dehydratation and $Al_2SiO_5$ triple points

(andalusite-And, sillimanite-Sil and kyanite-Ky) after Pattison (1992). Samples from both belts are projected in base of temperature obtained from average of semi-empirical thermometers (Inoue et al., 2009, 2018; Lanari et al., 2014) and *b* parameter measured value. The horizontal bar on each sample represents the range of average temperature values.

Fig. 10. (a-f) *P-T* diagrams shows results of chlorite + white mica + quartz + $H_2O$ equilibrium calculations for $Chl_1$-$Wm_2$ pairs, associated to $S_1$ development, for two samples of the Western Belt (a-c) and two samples from the Eastern Belt (d-f). (g-h) Thermometer method from Dubacq et al. (2010) applied to samples from the Western Belt (FSL-31009a2, FSL-31013a1 and FSL-31016a) and the Eastern Belt (FSL-31035a, FSL-31034a3 and FSL-31032a). In each sample, the *P-T* lines calculated were projected and constrained with solid lines with different colours (e.g., FSL-31009a2 with blue line). For more details, consult the text and Table 4.

Table 1. Summary of the clay minerals identified in the <2µm fraction of the analysed samples. Kübler index (KI; Δ°2θ) and white mica b (Å) parameter values are also shown. X: present but without quantification; Tr: traces. AD: air-dried samples; EG: glycolated samples.

| *Samples* | Wm | Chl | Kln | Qz | I/S (R0) | I/S (R1) | I/S (R3) | Gth | $KI_{CIS}$ AD <2µm | $KI_{CIS}$ EG <2µm | $KI_{CIS}$ 2-10 µm | $KI_{CIS}$ 10-20 µm | White mica *b* parameter | Observations |
|---|---|---|---|---|---|---|---|---|---|---|---|---|---|---|
| **Western Belt** | | | | | | | | | | | | | | |
| **FSL31008a1** | 47 | 20 | - | - | 33 | - | - | Tr | 0.42 | - | - | - | - | - |
| **FSL31008a2** | 58 | 18 | - | - | 24 | - | - | - | 0.35 | 0.34 | - | - | 9.014 | Bt; $S_1$ |
| **FSL31007a1** | 77 | - | 23 | - | - | - | - | Tr | 0.28 | 0.28 | - | - | 9.018 | Bt; $S_1$ |
| **FSL31009a1** | 75 | 24 | - | - | 1 | - | - | - | 0.28 | 0.25 | - | - | 9.019 | $S_1$ |
| **FSL31009a2*** | 89 | 1 | 10 | X | Tr | - | - | - | 0.28 | 0.25 | 0.23 | 0.23 | 9.019 | Bt; $S_1$ |
| **FSL31010a*** | 80 | | 20 | X | - | - | - | Tr | 0.23 | 0.23 | 0.23 | 0.21 | 9.006 | $S_1$ |
| **FSL31012a** | 59 | - | 41 | X | - | - | - | X | 0.19 | - | - | - | 9.022 | $S_1 \pm S_2$ |
| **FSL31013a1*** | 22 | 2 | 28 | - | 1 | 28 | 29 | X | 0.60 | 0.45 | 0.24 | 0.21 | 9.025 | Bt; $S_1 \pm S_2$ |
| **FSL31014a** | 31 | 14 | 55 | - | - | - | - | X | 0.18 | - | - | - | 9.017 | $S_1$ |
| **FSL31016a*** | 68 | 3 | 29 | | - | - | - | X | 0.21 | 0.21 | 0.23 | 0.20 | 9.020 | Bt; $S_1$-$S_2$ |
| **Eastern Belt** | | | | | | | | | | | | | | |
| **FSL31032a*** | 60 | 12 | - | - | 28 | - | - | - | 0.24 | 0.22 | 0.23 | 0.22 | 9.003 | Bt; $S_1$-$S_2$ |
| **FSL31033a1** | 62 | 6 | 3 | - | 29 | - | - | - | 0.21 | 0.21 | - | - | 9.008 | $S_1$ |
| **FSL31034a1** | - | - | - | - | - | - | - | - | 0.21 | - | - | - | 9.013 | $S_1$ |
| **FSL31034a2** | 91 | - | Tr | - | 9 | - | - | - | 0.24 | 0.27 | - | - | - | $S_1$ |
| **FSL31034a3*** | 84 | 2 | - | - | 14 | - | - | - | 0.23 | 0.24 | 0.24 | 0.22 | 9.011 | $S_1$ |
| **FSL31034a4** | 87 | 13 | - | - | Tr | - | - | - | 0.26 | 0.26 | - | - | 9.014 | $S_1$ |
| **FSL31034a5** | - | - | - | - | - | - | - | - | 0.19 | 0.19 | - | - | 9.020 | $S_1 \pm S_2$ |
| **FSL31035a*** | 20 | 65 | 1 | - | 14 | - | - | - | 0.25 | 0.25 | 0.23 | 0.21 | 9.017 | $S_1$ |
| **FSL31036a2** | 79 | 2 | - | | 20 | - | - | - | 0.20 | 0.19 | - | - | 9.020 | $S_{1\pm}S_2$ |
| **FSL31037a*** | 84 | 13 | - | - | 3 | - | - | - | 0.26 | 0.23 | 0.22 | 0.2 | 9.017 | $S_1$-$S_2$ |
| **FSL31039a1** | 17 | - | 83 | - | - | - | - | - | - | - | - | - | 9.019 | Bt; $S_1$-$S_2$ |
| **FSL31039a2** | 73 | 7 | Tr | - | 20 | - | - | - | - | - | - | - | 9.018 | Bt; $S_1$-$S_2$ |

** Samples selected for electron microprobe analysis.*

Table 2. Mean composition for chlorite, white mica and biotite in each sample.

| Samples | Western Belt | | | | | | Eastern Belt | | | | | | | | | |
|---|---|---|---|---|---|---|---|---|---|---|---|---|---|---|---|---|
| | FSL-31009a2 | | FSL-31010a | | FSL-31016a | | FSL-31037a | | FSL-31035a | | FSL-31034a3 | | FSL-31032a | | | |
| Mineral, textural variety and number of analyses | Chl1 (S1) (n=10) | | Chl1 (S1) (n=14) | | Chl1 (S1) (n=14) | | Chl1 (S1) (n=5) | | Chl1 (S1) (n=13) | | Chl1 (S1) (n=15) | | Chl1 (S1) (n=34) | | Chl2 (S2) (n=16) | |
| | Mean | S.d. | Mean | S.d. | Mean | S.d. | Mean | S.d. | Mean | S.d. | Mean | S.d. | Mean | S.d. | Mean | S.d. |
| ***Wt(%)*** | | | | | | | | | | | | | | | | |
| $SiO_2$ | 24.33 | 0.74 | 23.40 | 0.58 | 24.77 | 0.44 | 26.52 | 0.43 | 24.60 | 0.53 | 24.41 | 0.25 | 24.66 | 0.34 | 24.76 | 0.51 |
| $TiO_2$ | 0.05 | 0.05 | 0.07 | 0.03 | 0.06 | 0.05 | 0.09 | 0.02 | 0.07 | 0.04 | 0.06 | 0.05 | 0.08 | 0.07 | 0.08 | 0.08 |
| $Al_2O_3$ | 22.99 | 0.36 | 22.93 | 0.77 | 22.68 | 0.23 | 22.54 | 0.80 | 22.13 | 0.34 | 22.52 | 0.24 | 22.24 | 0.41 | 22.15 | 0.33 |
| FeO | 28.07 | 0.82 | 32.19 | 0.63 | 26.80 | 0.92 | 20.25 | 0.21 | 27.02 | 0.42 | 29.56 | 0.50 | 25.10 | 0.64 | 25.21 | 0.55 |
| MnO | 0.11 | 0.07 | 0.24 | 0.08 | 0.33 | 0.17 | 0.33 | 0.02 | 0.32 | 0.03 | 0.15 | 0.04 | 0.10 | 0.04 | 0.11 | 0.03 |
| MgO | 12.36 | 0.32 | 9.11 | 0.37 | 13.45 | 0.25 | 17.39 | 0.59 | 12.90 | 0.36 | 10.62 | 0.44 | 14.32 | 0.31 | 14.28 | 0.25 |
| CaO | 0.02 | 0.03 | 0.02 | 0.03 | 0.04 | 0.05 | 0.02 | 0.03 | 0.02 | 0.02 | 0.00 | 0.00 | 0.00 | 0.01 | 0.01 | 0.01 |
| $Na_2O$ | 0.01 | 0.02 | 0.04 | 0.04 | 0.01 | 0.01 | 0.02 | 0.02 | 0.02 | 0.03 | 0.02 | 0.03 | 0.02 | 0.03 | 0.01 | 0.02 |
| $K_2O$ | 0.03 | 0.04 | 0.03 | 0.03 | 0.03 | 0.03 | 0.24 | 0.13 | 0.10 | 0.08 | 0.03 | 0.03 | 0.07 | 0.08 | 0.09 | 0.11 |
| ***Apfu (14 oxygen)*** | | | | | | | | | | | | | | | | |
| Si | 2.59 | 0.07 | 2.55 | 0.05 | 2.62 | 0.04 | 2.72 | 0.02 | 2.64 | 0.03 | 2.64 | 0.02 | 2.63 | 0.03 | 2.64 | 0.04 |
| Ti | 0.00 | 0.00 | 0.01 | 0.00 | 0.00 | 0.00 | 0.01 | 0.00 | 0.01 | 0.00 | 0.00 | 0.00 | 0.01 | 0.01 | 0.01 | 0.01 |
| Al | 2.89 | 0.06 | 2.95 | 0.08 | 2.82 | 0.04 | 2.73 | 0.06 | 2.79 | 0.03 | 2.87 | 0.04 | 2.80 | 0.05 | 2.78 | 0.05 |
| Fe total | 2.50 | 0.07 | 2.94 | 0.08 | 2.37 | 0.08 | 1.74 | 0.02 | 2.42 | 0.04 | 2.67 | 0.05 | 2.24 | 0.06 | 2.25 | 0.05 |
| Mn | 0.01 | 0.01 | 0.02 | 0.01 | 0.03 | 0.02 | 0.03 | 0.00 | 0.03 | 0.00 | 0.01 | 0.00 | 0.01 | 0.00 | 0.01 | 0.00 |
| Mg | 1.96 | 0.05 | 1.48 | 0.05 | 2.12 | 0.03 | 2.66 | 0.12 | 2.06 | 0.06 | 1.71 | 0.07 | 2.28 | 0.05 | 2.27 | 0.04 |
| Ca | 0.00 | 0.00 | 0.00 | 0.00 | 0.00 | 0.01 | 0.00 | 0.00 | 0.00 | 0.00 | 0.00 | 0.00 | 0.00 | 0.00 | 0.00 | 0.00 |
| Na | 0.00 | 0.00 | 0.01 | 0.01 | 0.00 | 0.00 | 0.00 | 0.00 | 0.00 | 0.01 | 0.00 | 0.01 | 0.00 | 0.01 | 0.00 | 0.00 |
| K | 0.00 | 0.01 | 0.00 | 0.00 | 0.00 | 0.00 | 0.03 | 0.02 | 0.01 | 0.01 | 0.00 | 0.00 | 0.01 | 0.01 | 0.01 | 0.01 |
| XMg=Fe/(Fe+Mg) | 0.44 | 0.01 | 0.34 | 0.01 | 0.47 | 0.01 | 0.60 | 0.01 | 0.46 | 0.01 | 0.39 | 0.01 | 0.50 | 0.01 | 0.50 | 0.01 |
| *Vacancies* | | | | | | | | | | | | | | | | |
| $(Al^{VI} - Al^{IV} - Na - K)/2$ | 0.04 | 0.05 | 0.03 | 0.03 | 0.03 | 0.03 | 0.08 | 0.04 | 0.03 | 0.03 | 0.08 | 0.01 | 0.03 | 0.02 | 0.03 | 0.02 |
| $(Al^{VI}-Al^{IV})/2$ | 0.03 | 0.05 | 0.03 | 0.03 | 0.03 | 0.03 | 0.09 | 0.05 | 0.03 | 0.03 | 0.08 | 0.01 | 0.03 | 0.03 | 0.03 | 0.02 |
| ***Vacancies for Fe total = FeO + $Fe_2O_3$*** | | | | | | | | | | | | | | | | |
| $XFe^{3+}/(Fe^{2+}+Fe^{3+})$ estimated | 0.18 | 0.05 | 0.22 | 0.04 | 0.20 | 0.01 | 0.20 | 0.00 | 0.20 | 0.01 | 0.19 | 0.02 | 0.20 | 0.01 | 0.21 | 0.02 |
| XMg=Mg/(Fe2 + Mg) | 0.49 | 0.02 | 0.39 | 0.02 | 0.53 | 0.01 | 0.66 | 0.01 | 0.51 | 0.01 | 0.44 | 0.02 | 0.56 | 0.01 | 0.56 | 0.01 |
| $6-(Fe^{2+}+Fe^{3+}+Mg+A^{VI})$ | 0.22 | 0.07 | 0.29 | 0.05 | 0.24 | 0.04 | 0.27 | 0.05 | 0.25 | 0.03 | 0.28 | 0.03 | 0.22 | 0.03 | 0.22 | 0.03 |
| $(Al^{VI} - Al^{IV} + Fe^{3+}-Na-K)/2$ | 0.19 | 0.08 | 0.25 | 0.05 | 0.20 | 0.03 | 0.20 | 0.04 | 0.20 | 0.03 | 0.26 | 0.02 | 0.19 | 0.02 | 0.19 | 0.02 |

Note: F and Cl contents were omitted in this table. Full analyses are listed in Table Supplementary 2. S.d.: standard deviation.

Table 2. *Continuation.*

| Samples | Western Belt | | | | | | | | | | Eastern Belt | | | | | | | | | |
|---|---|---|---|---|---|---|---|---|---|---|---|---|---|---|---|---|---|---|---|---|
| | FSL-31009a2 | | FSL-31010a | | FSL-31013a1 | | | | FSL-31016a | | | | FSL-31037a | | FSL-31035a | | FSL-31034a3 | | FSL-31032a | |
| Mineral and textural variety | Wm2 (S1) (n=12) | | Wm2 (S1) (n=24) | | Wm2 (S1) (n=11) | | Wm3 (S2) (n=6) | | Wm2 (S1) (n=23) | | Wm3 (S2) (n=26) | | Wm2 (S1) (n=22) | | Wm2 (S1) (n=19) | | Wm2 (S1) (n=43) | | Wm2 (S1) (n=31) | | Wm3 (S2) (n=18) | |
| | Mean | S.d. | Mean | S.d. | Mean | S.d. | Mean | S.d. | Mean | S.d. | Mean | S.d. | Mean | S.d. | Mean | S.d. | Mean | S.d. | Mean | S.d. | Mean | S.d. |
| Wt (%) | | | | | | | | | | | | | | | | | | | | | | |
| $SiO_2$ | 47.12 | 0.85 | 45.99 | 0.66 | 47.30 | 0.88 | 47.32 | 0.56 | 46.61 | 0.61 | 47.07 | 0.81 | 47.63 | 1.05 | 47.99 | 1.15 | 46.77 | 0.88 | 47.64 | 1.05 | 48.10 | 0.63 |
| $TiO_2$ | 0.3 | 0.1 | 0.2 | 0.0 | 0.4 | 0.0 | 0.4 | 0.1 | 0.4 | 0.1 | 0.4 | 0.0 | 0.4 | 0.1 | 0.3 | 0.0 | 0.2 | 0.1 | 0.3 | 0.1 | 0.3 | 0.1 |

| | | | | | | | | | | | | | | | | | | | | | | | |
|---|---|---|---|---|---|---|---|---|---|---|---|---|---|---|---|---|---|---|---|---|---|---|---|
| $Al_2O_3$ | 32.44 | 1.06 | 35.74 | 0.44 | 32.92 | 1.24 | 32.71 | 0.57 | 33.58 | 0.52 | 32.80 | 0.65 | 33.49 | 1.62 | 31.50 | 1.04 | 34.47 | 1.01 | 31.19 | 1.16 | 31.34 | 1.25 |
| FeO | 2.95 | 1.06 | 2.97 | 0.30 | 2.77 | 0.54 | 2.66 | 0.26 | 2.36 | 0.29 | 2.46 | 0.63 | 1.69 | 0.54 | 3.26 | 0.58 | 2.85 | 0.32 | 3.70 | 0.61 | 3.55 | 0.25 |
| MnO | 0.04 | 0.07 | 0.03 | 0.05 | 0.05 | 0.08 | 0.03 | 0.04 | 0.07 | 0.08 | 0.05 | 0.07 | 0.03 | 0.03 | 0.02 | 0.02 | 0.01 | 0.02 | 0.02 | 0.02 | 0.02 | 0.02 |
| MgO | 1.78 | 0.44 | 0.45 | 0.07 | 1.69 | 0.39 | 1.78 | 0.11 | 1.62 | 0.14 | 1.65 | 0.25 | 1.83 | 0.59 | 1.35 | 0.34 | 0.66 | 0.12 | 1.66 | 0.50 | 1.64 | 0.45 |
| CaO | 0.03 | 0.03 | 0.03 | 0.03 | 0.02 | 0.03 | 0.04 | 0.04 | 0.03 | 0.02 | 0.03 | 0.03 | 0.02 | 0.02 | 0.02 | 0.02 | 0.01 | 0.02 | 0.02 | 0.04 | 0.01 | 0.02 |
| $Na_2O$ | 0.29 | 0.08 | 0.71 | 0.08 | 0.24 | 0.09 | 0.25 | 0.07 | 0.32 | 0.05 | 0.26 | 0.07 | 0.26 | 0.11 | 0.33 | 0.07 | 0.49 | 0.12 | 0.21 | 0.07 | 0.24 | 0.07 |
| $K_2O$ | 10.11 | 0.46 | 9.45 | 0.39 | 10.17 | 0.47 | 10.50 | 0.10 | 10.12 | 0.29 | 10.04 | 0.43 | 9.68 | 0.35 | 10.12 | 0.37 | 9.83 | 0.24 | 10.20 | 0.38 | 10.17 | 0.30 |
| **Apfu *(11 oxygen)*** | | | | | | | | | | | | | | | | | | | | | | | |
| Si | 3.16 | 0.05 | 3.06 | 0.03 | 3.15 | 0.05 | 3.15 | 0.02 | 3.12 | 0.02 | 3.16 | 0.04 | 3.16 | 0.06 | 3.23 | 0.06 | 3.12 | 0.05 | 3.21 | 0.06 | 3.22 | 0.05 |
| Ti | 0.02 | 0.00 | 0.01 | 0.00 | 0.02 | 0.00 | 0.02 | 0.01 | 0.02 | 0.01 | 0.02 | 0.00 | 0.02 | 0.01 | 0.02 | 0.00 | 0.01 | 0.01 | 0.02 | 0.01 | 0.02 | 0.01 |
| Al | 2.56 | 0.07 | 2.80 | 0.04 | 2.59 | 0.10 | 2.57 | 0.04 | 2.65 | 0.04 | 2.69 | 0.04 | 2.62 | 0.12 | 2.50 | 0.08 | 2.71 | 0.07 | 2.48 | 0.09 | 2.47 | 0.09 |
| Fe total | 0.17 | 0.06 | 0.17 | 0.02 | 0.15 | 0.03 | 0.15 | 0.01 | 0.13 | 0.02 | 0.14 | 0.04 | 0.09 | 0.03 | 0.18 | 0.03 | 0.16 | 0.02 | 0.21 | 0.04 | 0.20 | 0.01 |
| Mn | 0.00 | 0.00 | 0.00 | 0.00 | 0.00 | 0.00 | 0.00 | 0.00 | 0.00 | 0.00 | 0.00 | 0.00 | 0.00 | 0.00 | 0.00 | 0.00 | 0.00 | 0.00 | 0.00 | 0.00 | 0.00 | 0.00 |
| Mg | 0.18 | 0.04 | 0.05 | 0.01 | 0.17 | 0.04 | 0.18 | 0.01 | 0.16 | 0.01 | 0.17 | 0.03 | 0.18 | 0.06 | 0.14 | 0.03 | 0.07 | 0.01 | 0.17 | 0.05 | 0.16 | 0.04 |
| Ca | 0.00 | 0.00 | 0.00 | 0.00 | 0.00 | 0.00 | 0.00 | 0.00 | 0.00 | 0.00 | 0.00 | 0.00 | 0.00 | 0.00 | 0.00 | 0.00 | 0.00 | 0.00 | 0.00 | 0.00 | 0.00 | 0.00 |
| Na | 0.04 | 0.01 | 0.09 | 0.01 | 0.03 | 0.01 | 0.03 | 0.01 | 0.04 | 0.01 | 0.03 | 0.01 | 0.03 | 0.01 | 0.04 | 0.01 | 0.06 | 0.02 | 0.03 | 0.01 | 0.03 | 0.01 |
| K | 0.87 | 0.04 | 0.80 | 0.03 | 0.87 | 0.04 | 0.91 | 0.01 | 0.86 | 0.03 | 0.86 | 0.04 | 0.82 | 0.03 | 0.87 | 0.03 | 0.84 | 0.02 | 0.88 | 0.03 | 0.87 | 0.03 |
| Cation sum | 6.99 | 0.03 | 6.98 | 0.03 | 6.98 | 0.03 | 7.00 | 0.01 | 6.99 | 0.02 | 6.97 | 0.04 | 6.93 | 0.02 | 6.97 | 0.03 | 6.97 | 0.03 | 6.99 | 0.03 | 6.98 | 0.02 |
| XMg=Mg/(Fe+Mg) | 0.52 | 0.03 | 0.21 | 0.03 | 0.52 | 0.04 | 0.54 | 0.03 | 0.55 | 0.03 | 0.55 | 0.04 | 0.66 | 0.05 | 0.42 | 0.04 | 0.29 | 0.04 | 0.44 | 0.05 | 0.44 | 0.06 |
| XNa = Na/(Na+K+Ca) | 0.04 | 0.01 | 0.10 | 0.01 | 0.03 | 0.01 | 0.03 | 0.01 | 0.05 | 0.01 | 0.04 | 0.01 | 0.04 | 0.02 | 0.05 | 0.01 | 0.07 | 0.02 | 0.03 | 0.01 | 0.03 | 0.01 |
| ***Calculated b parameter (Å)*** | | | | | | | | | | | | | | | | | | | | | | | |
| $b$ = 8.9931 + 0.0440 Σ (Mg + Fe) | 9.023 | 0.09 | 9.012 | 0.02 | 9.021 | 0.06 | 9.022 | 0.01 | 9.019 | 0.02 | 9.020 | 0.05 | 9.017 | 0.08 | 9.021 | 0.06 | 9.013 | 0.02 | 9.026 | 0.07 | 9.025 | 0.05 |
| $b$ = 9.1490 - 0.0258 Σ ($A1^{IV}$ + $A1^{VI}$) | 9.017 | 0.04 | 9.004 | 0.02 | 9.016 | 0.05 | 9.016 | 0.02 | 9.012 | 0.02 | 9.015 | 0.02 | 9.014 | 0.06 | 9.020 | 0.04 | 9.009 | 0.04 | 9.021 | 0.04 | 9.021 | 0.05 |
| $b$ = 8.5966 + 0.0666 Si | 9.018 | 0.07 | 9.004 | 0.04 | 9.017 | 0.07 | 9.017 | 0.03 | 9.012 | 0.03 | 9.017 | 0.05 | 9.018 | 0.09 | 9.026 | 0.08 | 9.012 | 0.07 | 9.024 | 0.08 | 9.026 | 0.06 |
| ***b parameter from DRX*** | 9.019 | | 9.006 | | 9.025 | | | | 9.020 | | | | 9.017 | | 9.017 | | 9.011 | | | 9.003 | | | |

Note: F and Cl contents were omitted in this table. Full analyses are listed in Table Supplementary 2. S.d.: standard deviation.

Table 3. Summary of temperatures (ºC) calculated in chlorites with empirical and semi-empirical methods.

| Samples *(ordered from west to east)* | **Western Belt** | | | **Eastern Belt** | | | | |
|---|---|---|---|---|---|---|---|---|
| | FSL-31009a2 ($S_1$) | FSL-31010a ($S_1$) | FSL-31016a ($S_1$) | FSL-31037a ($S_1$) | FSL-31035a ($S_1$) | FSL-31034a3 ($S_1$) | FSL-31032a ($S_1$) | FSL-31032a ($S_2$) |
| ***Empirical thermometry*** | | | | | | | | |
| Catherlineau (1988) (C88) | 391±22 (n=10) | 403±17 (n=14) | 384±13 (n=14) | 349±8 (n=5) | 377±11 (n=13) | 376±6 (n=15) | 379±8 (n=34) | 376±14 (n=16) |
| Jowett (1991) (J91) | 398±22 (n=10) | 413±17 (n=14) | 389±13 (n=14) | 351±8 (n=5) | 383±11 (n=13) | 384±6 (n=15) | 383±8 (n=34) | 381±14 (n=16) |
| ***Semi-empirical thermometry – Fe total as FeO*** | | | | | | | | |
| Bourdelle et al. (2013) (B13) | 316±47 (n=4) | 361±31 (n=4) | 326±23 (n=3) | 261±21 (n=3) | 348±45 (n=4) | 346±30 (n=15) | 366±42 (n=7) | 343±34 (n=3) |
| Inoue et al. (2018) (I18) | 356±65 (n=8) | 367±67 (n=14) | 351±44 (n=14) | 283±32 (n=5) | 332±27 (n=13) | 318±10 (n=15) | 349±23 (n=32) | 348±28 (n=16) |
| ***Semi-empirical thermometry – Fe total as FeO + $Fe_2O_3$*** | | | | | | | | |
| Inoue et al. (2009) (I09) | 386±66 (n=10) | 372±33 (n=14) | 364±35 (n=14) | 301±36 (n=5) | 351±30 (n=13) | 331±16 (n=15) | 367±20 (n=32) | 364±30 (n=16) |
| Lanari et al. (2014) (La14) | 380±60 (n=7) | 416±43 (n=14) | 405±48 (n=14) | 357±31 (n=5) | 400±39 (n=13) | 352±19 (n=15) | 403±23 (n=32) | 398±29 (n=16) |

Notes: errors are expressed as one sigma (1σ). Number of analysis is signalled with "n".

Table 4. Temperatures and pressures calculated in chlorites ($Chl_1$) – white mica ($Wm_2$) pairs from Chl-Wm/WmH-Qz-$H_2O$ equilibrium. Also, temperatures were estimated at fixed pressure from WmH-Qz-$H_2O$ equilibrium followed the Dubacq et al. (2010) method. WmH= white mica with interlayer water.

| Sample | Chl-Wm-Qz-$H_2O$ (1) | Chl-WmH-Qz-$H_2O$ (2) and WmH-Qz-$H_2O$ (3) equilibria |
|---|---|---|
| ***Western Belt*** | | |
| *FSL-31009a2 (S1)* | *Analysis Chl-22 and Wm-40*<br>317.2º C – 5.09 kbar. $XFe^{3+}$ Chl=0.23; $XFe^{3+}$ Wm=0.49 | Chl-WmH-Qz-$H_2O$<br>*Analysis Chl-22 and Wm-40*<br>358.6º C – *8.86 kbar*<br>$XFe^{3+}$ Chl=0.14; $XFe^{3+}$ Wm=0.44<br><br>WmH-Qz-$H_2O$<br>($XFe^{3+}$ in Wm = 0.5)<br>Pressure of 5 kbar and n=12<br>*ca.* 340-420º C. |
| *FSL-31016a (S1)* | *Analysis Chl-45 and Wm-57*<br>476.1º C – 2.61 kbar. $XFe^{3+}$ Chl=0.11; $XFe^{3+}$ Wm=0.22<br><br>*Analysis Chl-51 and Wm-62*<br>480.2º C – 4.01 kbar. $XFe^{3+}$ Chl=0.10; $XFe^{3+}$ Wm=0.18<br><br>*Analysis Chl-2 and Wm-14*<br>455.1º C – 3.87 kbar. $XFe^{3+}$ Chl=0.06; $XFe^{3+}$ Wm=0.16<br><br>*Analysis Chl-43 and Wm-35*<br>377.2º C – 4.60 kbar. $XFe^{3+}$ Chl=0.17; $XFe^{3+}$ Wm=0.46<br><br>*Analysis Chl-3 and Wm-12*<br>365.2º C – 3.93 kbar. $XFe^{3+}$ Chl=0.1; $XFe^{3+}$ Wm=0.4<br><br>*Analysis Chl-5 and Wm-11*<br>445.5º C – 2.53 kbar. $XFe^{3+}$ Chl=0.08; $XFe^{3+}$ Wm=0.14 | Chl-WmH-Qz-$H_2O$<br>*Analysis Chl-2 and Wm-14*<br>375.1º C – 4.85 kbar<br>$XFe^{3+}$ Chl=0.22; $XFe^{3+}$ Wm=0.43<br><br>WmH-Qz-$H_2O$<br>($XFe^{3+}$ in Wm = 0.5)<br>Pressure of 5 kbar and n=23<br>*ca.* 370-430º C. |
| ***Eastern Belt*** | | |
| *FSL-31034a3 (S1)* | *Analysis Chl-41 and Wm-39*<br>407.9º C – 4.29 kbar. $XFe^{3+}$ Chl=0.15; $XFe^{3+}$ Wm=0.65<br><br>*Analysis Chl-43 and Wm-38*<br>401.1º C – 4.68 kbar. $XFe^{3+}$ Chl=0.21; $XFe^{3+}$ Wm=0.65 | WmH-Qz-$H_2O$<br>($XFe^{3+}$ in Wm = 0.5)<br>Pressure of 4.5 kbar and n=43<br>*ca.* 330-420º C. |
| *FSL-31032a (S1)* | *$XFe^{3+}$ was adjusted to >0.15 for to achieve the equilibrium*<br><br>*Analysis Chl-7 and Wm-59r*<br>361.6º C – 3.5 kbar. $XFe^{3+}$ Chl=0.15; $XFe^{3+}$ Wm=0.67<br><br>*Analysis Chl-1 and Wm-60*<br>370.5º C – 3.3 kbar. $XFe^{3+}$ Chl=0.19; $XFe^{3+}$ Wm=0.69<br><br>*Analysis Chl-20 and Wm-67r*<br>380.0º C – 3.6 kbar. $XFe^{3+}$ Chl=0.15; $XFe^{3+}$ Wm=0.65 | Chl-WmH-Qz-$H_2O$<br>*Analysis Chl-20 and Wm-67r*<br>353.8º C – 3.4 kbar<br>$XFe^{3+}$ Chl=0.22; $XFe^{3+}$ Wm=0.68<br><br>WmH-Qz-$H_2O$<br>($XFe^{3+}$ in Wm = 0.5)<br>Pressure of 3.5 kbar and n=31<br>*ca.* 285-370º C. |
| *FSL-31032a* | *$XFe^{3+}$ was adjusted to >0.15 for to achieve the* | WmH-Qz-$H_2O$ |

| | | |
|---|---|---|
| *(S2)* | *equilibrium*<br><br>*Analysis Chl-90 and Wm-106r*<br>432.9º C – 3.2 kbar. $XFe^{3+}$ Chl=0.15; $XFe^{3+}$ Wm=0.68<br><br>*Analysis Chl-92r and Wm-109r*<br>442.1º C – 2.8 kbar. $XFe^{3+}$ Chl=0.157; $XFe^{3+}$ Wm=0.69 | ($XFe^{3+}$ in Wm = 0.5)<br>Pressure of 3 kbar and n=18<br>*ca.* 300-370º C. |

(1) The calculations were made with the solution models of chlorite from Vidal (2005, 2006) and white mica of Parra et al. (2002). (2) The calculations were made with chlorite model from Vidal (2005, 2006) and white mica (WmH) model from Dubacq et al. (2010). (3) WmH-Qz-$H_2O$ thermometer method from Dubacq et al. (2010) for variable hydration status in white mica. For FSL-31013a1 sample, a temperature of 340-420º C was estimated at 5 kbar. For the FSL-31035a a temperature of 310-390º C was estimated at 4.5 kbar. The pressure in both samples was estimated from correlation to near samples: FSL-31016a and FSL-31034a3 respectively.

**Highlights:**

- Multiproxy analysis to characterize units with low-grade metamorphism
- Advantages of a joint use of crystallochemical indexes and geothermobarometric calculations
- Kübler index and white mica *b* parameter as crystallochemical indexes
- Chlorite thermometers and multi-equilibrium as geothermobarometric methods
- Similar *P*-*T* conditions are obtained from both methods

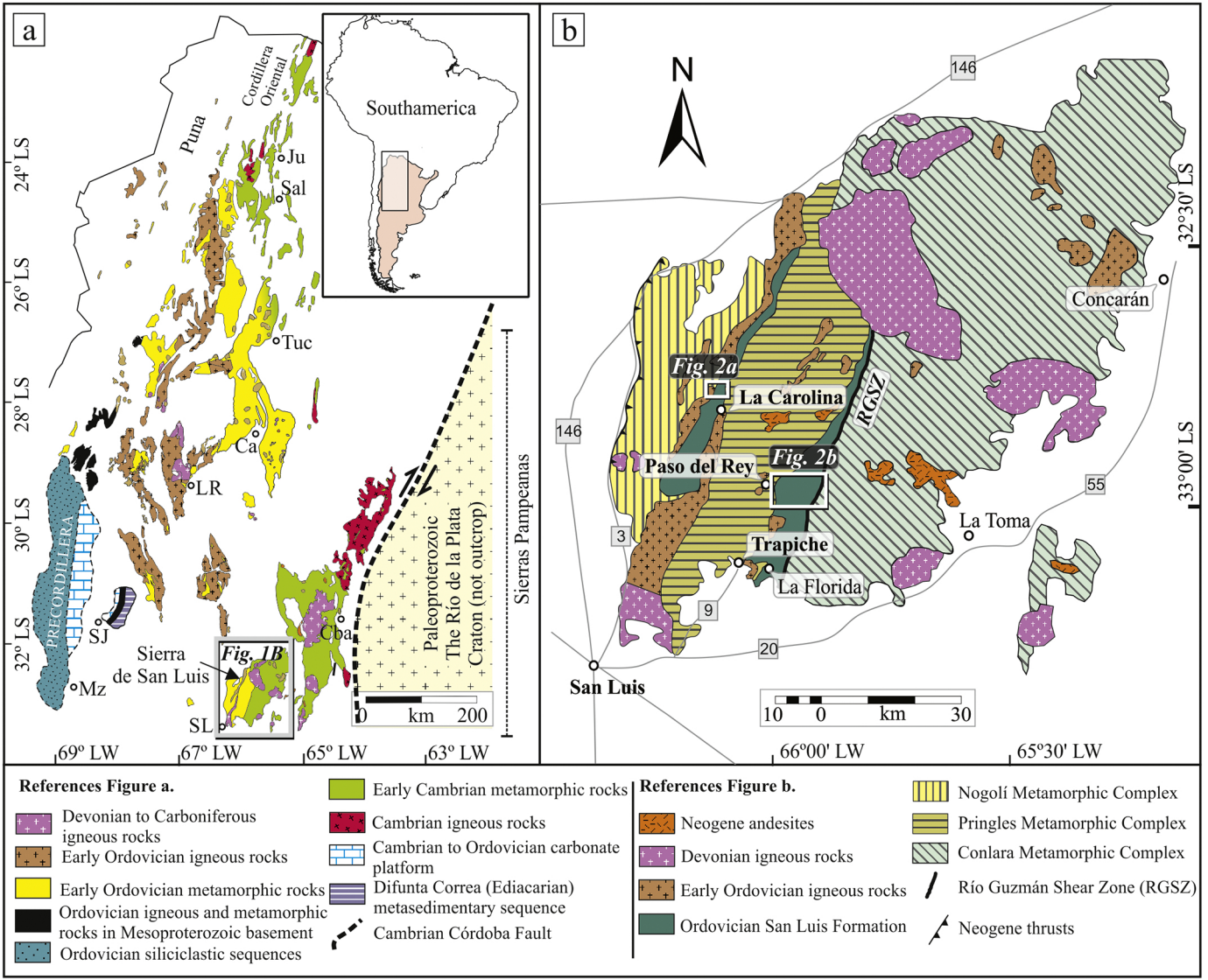
a
Puna
Cordillera Oriental
Southamerica
Ju
Sal
Tuc
Ca
LR
PRECORDILLERA
SJ
Mz
Sierra de San Luis
Fig. 1B
SL
Cba
Paleoproterozoic The Río de la Plata Craton (not outcrop)
Sierras Pampeanas
0 km 200
24° LS
26° LS
28° LS
30° LS
32° LS
69° LW
67° LW
65° LW
63° LW
b
N
146
Concarán
32°30' LS
Fig. 2a
La Carolina
RGSZ
146
Paso del Rey
Fig. 2b
55
33°00' LS
3
La Toma
Trapiche
La Florida
9
20
San Luis
10 0 km 30
66°00' LW
65°30' LW
References Figure a.
Devonian to Carboniferous igneous rocks
Early Ordovician igneous rocks
Early Ordovician metamorphic rocks
Ordovician igneous and metamorphic rocks in Mesoproterozoic basement
Ordovician siliciclastic sequences
Early Cambrian metamorphic rocks
Cambrian igneous rocks
Cambrian to Ordovician carbonate platform
Difunta Correa (Ediacarian) metasedimentary sequence
Cambrian Córdoba Fault
References Figure b.
Neogene andesites
Devonian igneous rocks
Early Ordovician igneous rocks
Ordovician San Luis Formation
Nogolí Metamorphic Complex
Pringles Metamorphic Complex
Conlara Metamorphic Complex
Río Guzmán Shear Zone (RGSZ)
Neogene thrusts

Figure 1

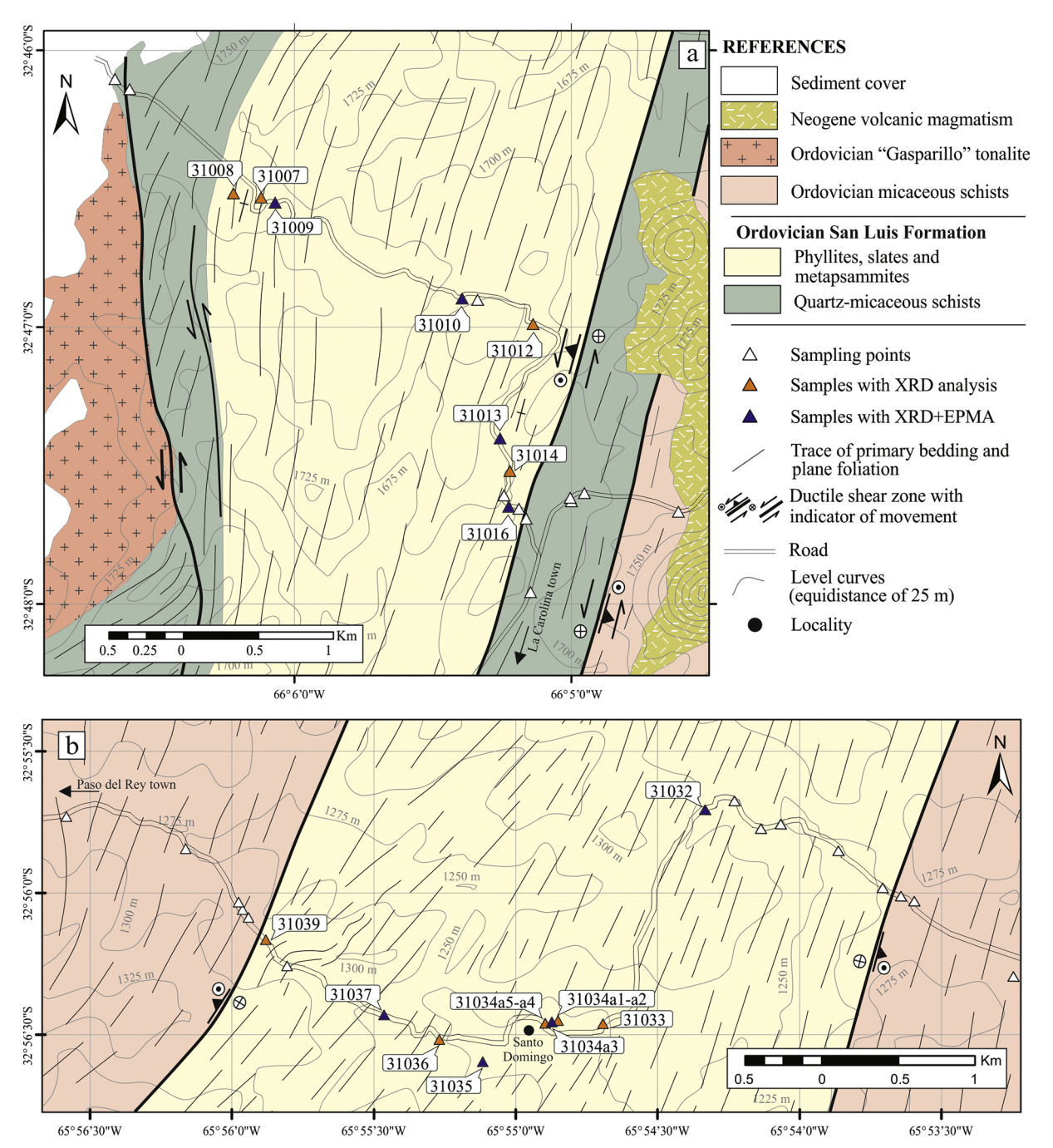
a
REFERENCES
Sediment cover
Neogene volcanic magmatism
Ordovician "Gasparillo" tonalite
Ordovician micaceous schists
Ordovician San Luis Formation
Phyllites, slates and metapsammites
Quartz-micaceous schists
Sampling points
Samples with XRD analysis
Samples with XRD+EPMA
Trace of primary bedding and plane foliation
Ductile shear zone with indicator of movement
Road
Level curves (equidistance of 25 m)
Locality
31008
31007
31009
31010
31012
31013
31014
31016
La Carolina town
32° 46'0"S
32° 47'0"S
32° 48'0"S
66° 6'0"W
66° 5'0"W
b
Paso del Rey town
31032
31039
31037
31034a5-a4
31034a1-a2
31033
31034a3
31036
31035
Santo Domingo
32° 55'30"S
32° 56'0"S
32° 56'30"S
65° 56'30"W
65° 56'0"W
65° 55'30"W
65° 55'0"W
65° 54'30"W
65° 54'0"W
65° 53'30"W

Figure 2

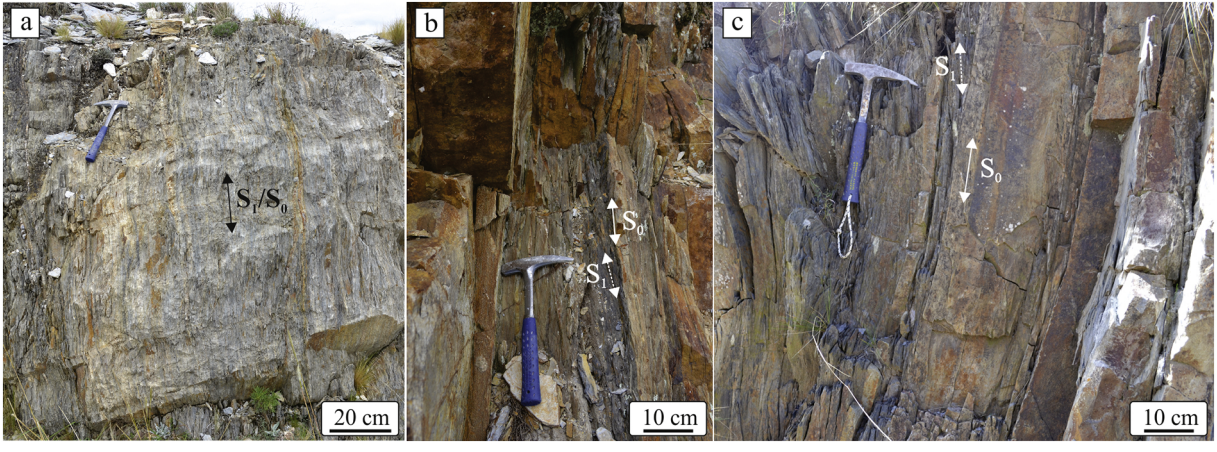


Figure 3

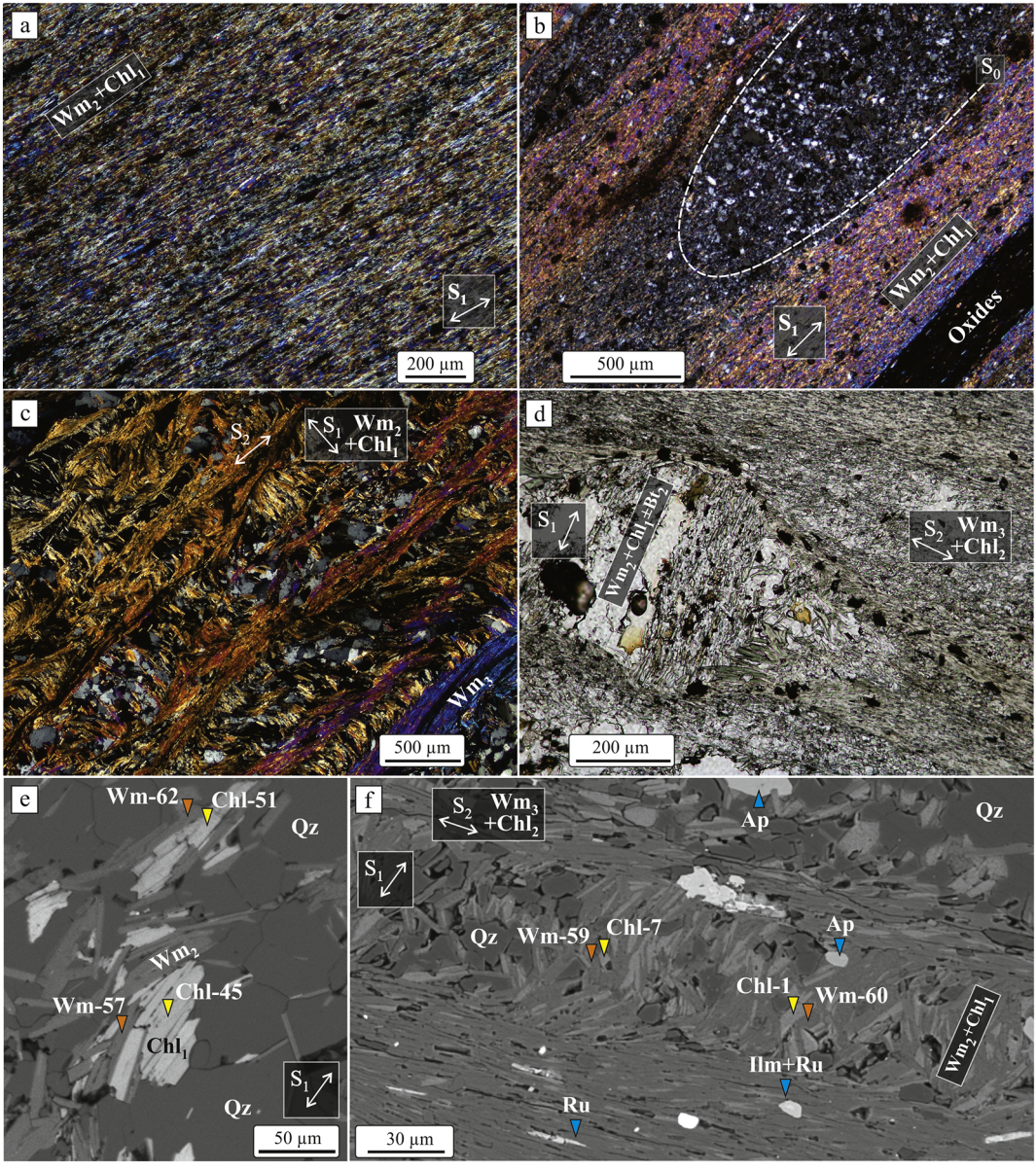
a
Wm2+Chl1
S1
200 μm
b
S0
Wm2+Chl1
S1
Oxides
500 μm
c
S2
S1 Wm2 +Chl1
Wm3
500 μm
d
S1
Wm2+Chl1±Bt2
S2 Wm3 +Chl2
200 μm
e
Wm-62
Chl-51
Qz
Wm2
Chl-45
Wm-57
Chl1
S1
Qz
50 μm
f
S2 Wm3 +Chl2
Ap
Qz
S1
Qz
Wm-59
Chl-7
Ap
Chl-1
Wm-60
Wm2+Chl1
Ilm+Ru
Ru
30 μm

Figure 4

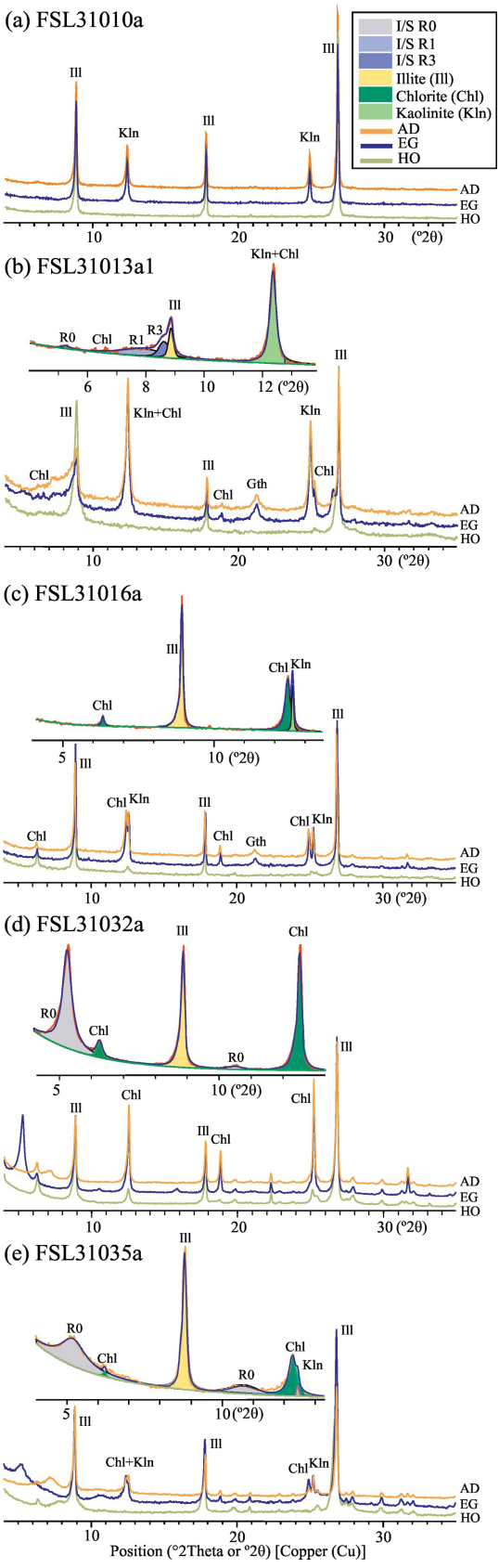
(a) FSL31010a
I/S R0
I/S R1
I/S R3
Illite (Ill)
Chlorite (Chl)
Kaolinite (Kln)
AD
EG
HO
Ill
Kln
Ill
Kln
Ill
AD
EG
HO
10
20
30 (°2θ)
(b) FSL31013a1
Kln+Chl
Ill
R0
Chl
R1
R3
6
8
10
12 (°2θ)
Ill
Ill
Kln+Chl
Kln
Chl
Ill
Chl
Gth
Chl
AD
EG
HO
10
20
30 (°2θ)
(c) FSL31016a
Ill
Chl
Kln
Chl
5
10 (°2θ)
Ill
Ill
Chl
Kln
Ill
Chl
Chl
Kln
Chl
Gth
AD
EG
HO
10
20
30 (°2θ)
(d) FSL31032a
Ill
Chl
R0
Chl
5
10 (°2θ)
R0
Ill
Ill
Chl
Ill
Chl
Chl
AD
EG
HO
10
20
30 (°2θ)
(e) FSL31035a
Ill
R0
Chl
Chl
Kln
R0
5
10 (°2θ)
Ill
Ill
Chl+Kln
Ill
Chl
Kln
AD
EG
HO
10
20
30
Position (°2Theta or °2θ) [Copper (Cu)]

Figure 5

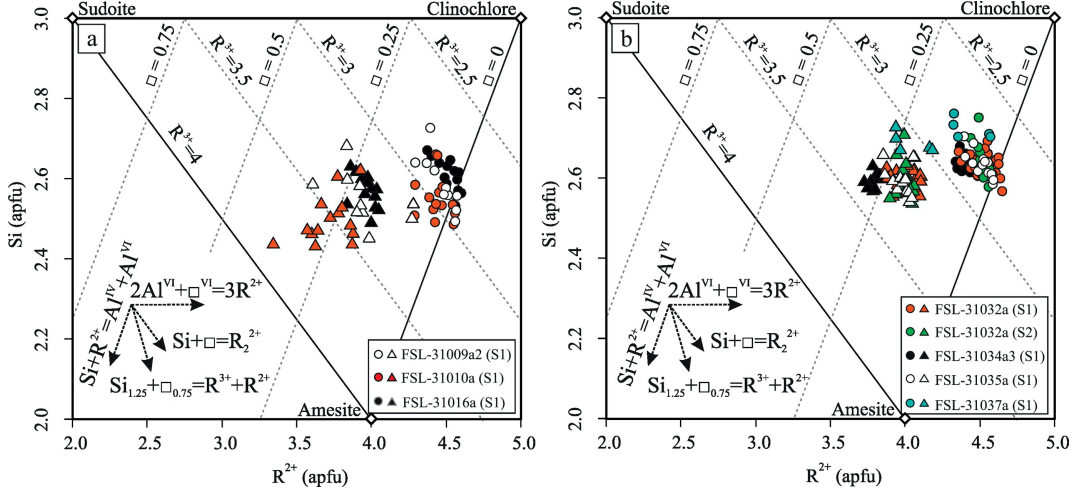
Sudoite
Clinochlore
Amesite
a
b
□ = 0.75
□ = 0.5
□ = 0.25
□ = 0
R3+=4
R3+=3.5
R3+=3
R3+=2.5
2Al^VI+□^VI=3R2+
Si+□=R2 2+
Si1.25+□0.75=R3++R2+
Si+R2+=Al^IV+Al^VI
Si (apfu)
R2+ (apfu)
FSL-31009a2 (S1)
FSL-31010a (S1)
FSL-31016a (S1)
FSL-31032a (S1)
FSL-31032a (S2)
FSL-31034a3 (S1)
FSL-31035a (S1)
FSL-31037a (S1)

Figure 6

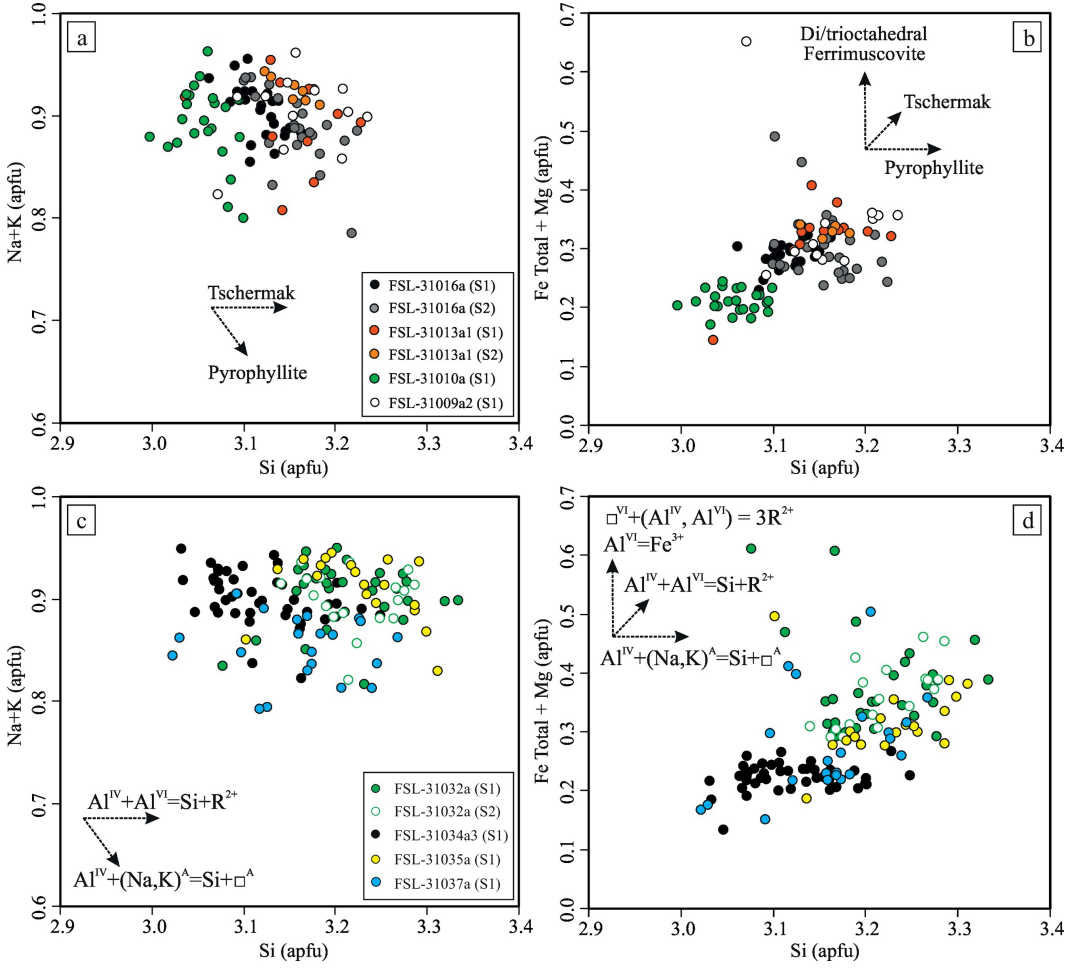
a
Na+K (apfu)
Si (apfu)
Tschermak
Pyrophyllite
FSL-31016a (S1)
FSL-31016a (S2)
FSL-31013a1 (S1)
FSL-31013a1 (S2)
FSL-31010a (S1)
FSL-31009a2 (S1)
b
Fe Total + Mg (apfu)
Si (apfu)
Di/trioctahedral
Ferrimuscovite
Tschermak
Pyrophyllite
c
Na+K (apfu)
Si (apfu)
Al^IV+Al^VI=Si+R^2+
Al^IV+(Na,K)^A=Si+□^A
FSL-31032a (S1)
FSL-31032a (S2)
FSL-31034a3 (S1)
FSL-31035a (S1)
FSL-31037a (S1)
d
Fe Total + Mg (apfu)
Si (apfu)
□^VI+(Al^IV, Al^VI) = 3R^2+
Al^VI=Fe^3+
Al^IV+Al^VI=Si+R^2+
Al^IV+(Na,K)^A=Si+□^A

Figure 7

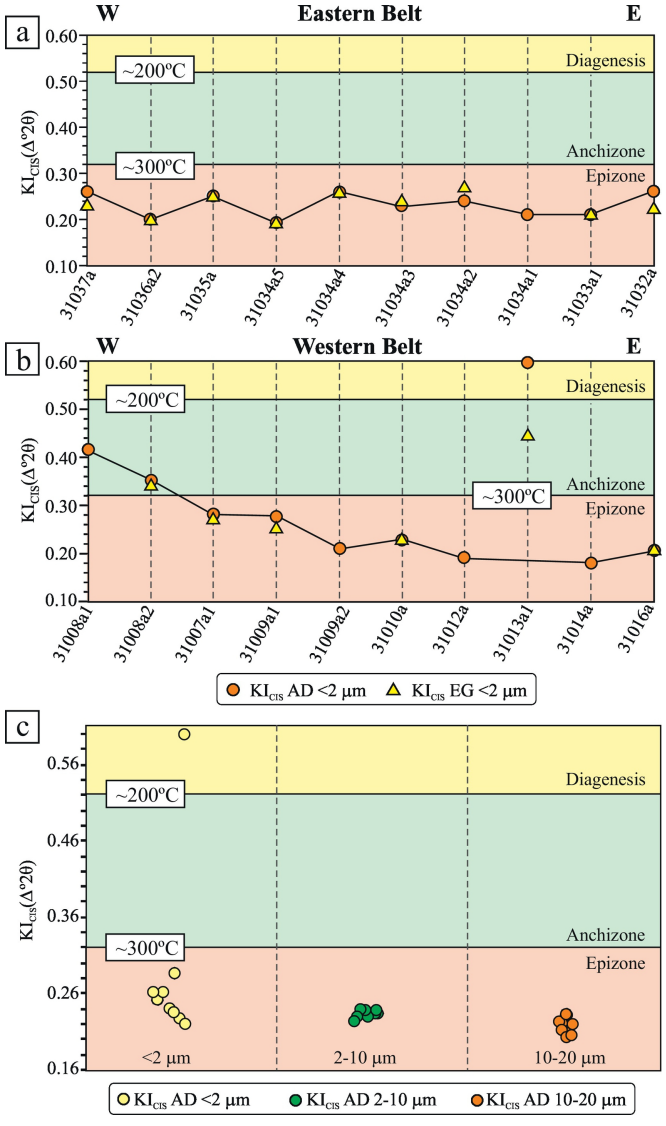
a
W
Eastern Belt
E
~200ºC
~300ºC
Diagenesis
Anchizone
Epizone
KI_CIS(Δº2θ)
0.60
0.50
0.40
0.30
0.20
0.10
31037a
31036a2
31035a
31034a5
31034a4
31034a3
31034a2
31034a1
31033a1
31032a
b
W
Western Belt
E
~200ºC
~300ºC
Diagenesis
Anchizone
Epizone
KI_CIS(Δº2θ)
0.60
0.50
0.40
0.30
0.20
0.10
31008a1
31008a2
31007a1
31009a1
31009a2
31010a
31012a
31013a1
31014a
31016a
KI_CIS AD <2 µm
KI_CIS EG <2 µm
c
~200ºC
~300ºC
Diagenesis
Anchizone
Epizone
KI_CIS(Δº2θ)
0.56
0.46
0.36
0.26
0.16
<2 µm
2-10 µm
10-20 µm
KI_CIS AD <2 µm
KI_CIS AD 2-10 µm
KI_CIS AD 10-20 µm

Figure 8

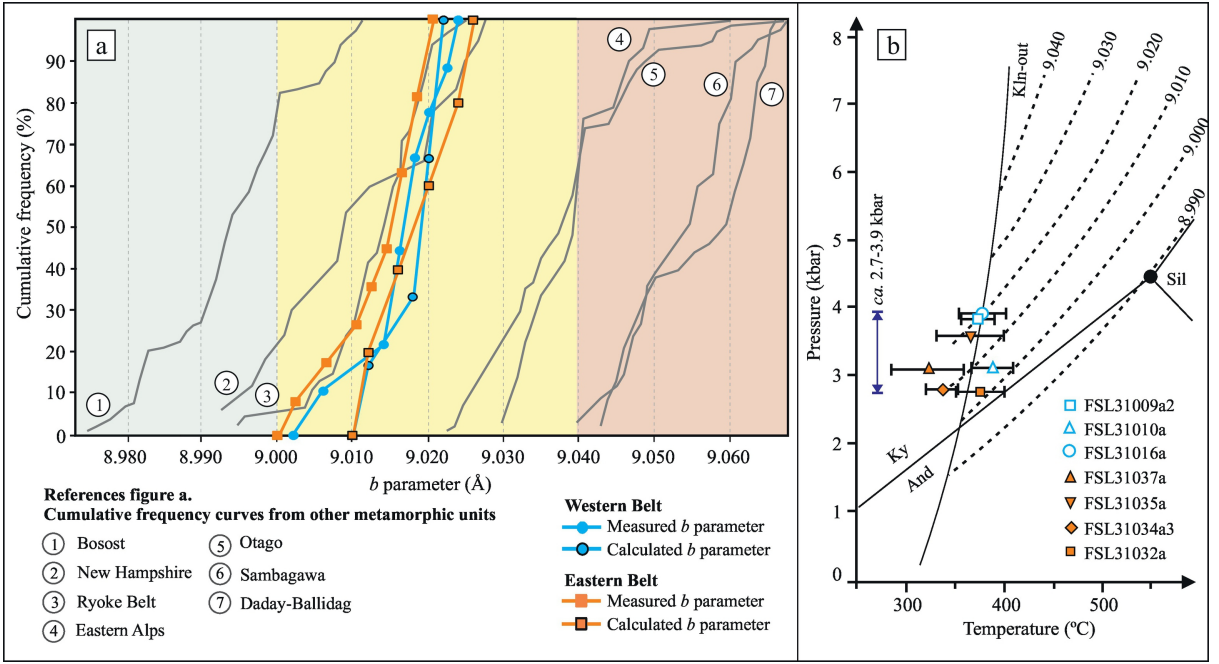
a
Cumulative frequency (%)
b parameter (Å)
8.980
8.990
9.000
9.010
9.020
9.030
9.040
9.050
9.060
References figure a.
Cumulative frequency curves from other metamorphic units
1 Bosost
2 New Hampshire
3 Ryoke Belt
4 Eastern Alps
5 Otago
6 Sambagawa
7 Daday-Ballidag
Western Belt
Measured b parameter
Calculated b parameter
Eastern Belt
Measured b parameter
Calculated b parameter
b
Pressure (kbar)
Temperature (ºC)
Kln-out
9.040
9.030
9.020
9.010
9.000
8.990
Sil
ca. 2.7-3.9 kbar
Ky
And
FSL31009a2
FSL31010a
FSL31016a
FSL31037a
FSL31035a
FSL31034a3
FSL31032a

Figure 9

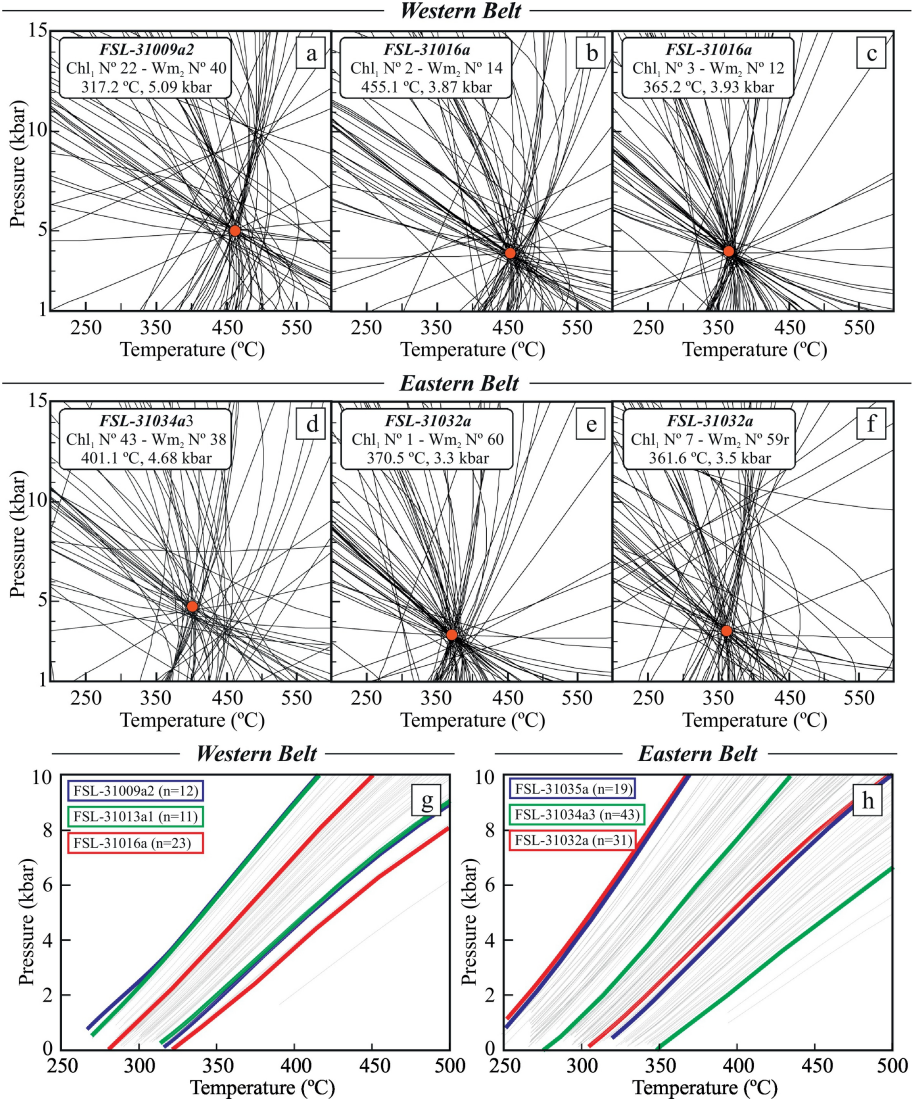
Western Belt
FSL-31009a2
Chl1 Nº 22 - Wm2 Nº 40
317.2 ºC, 5.09 kbar
a
FSL-31016a
Chl1 Nº 2 - Wm2 Nº 14
455.1 ºC, 3.87 kbar
b
FSL-31016a
Chl1 Nº 3 - Wm2 Nº 12
365.2 ºC, 3.93 kbar
c
Pressure (kbar)
Temperature (ºC)
Eastern Belt
FSL-31034a3
Chl1 Nº 43 - Wm2 Nº 38
401.1 ºC, 4.68 kbar
d
FSL-31032a
Chl1 Nº 1 - Wm2 Nº 60
370.5 ºC, 3.3 kbar
e
FSL-31032a
Chl1 Nº 7 - Wm2 Nº 59r
361.6 ºC, 3.5 kbar
f
Western Belt
FSL-31009a2 (n=12)
FSL-31013a1 (n=11)
FSL-31016a (n=23)
g
Eastern Belt
FSL-31035a (n=19)
FSL-31034a3 (n=43)
FSL-31032a (n=31)
h

Figure 10